Structural remodeling of target-SNARE protein complexes by NSF enables synaptic transmission

K. Ian White[1,2,3,4,5,**], Yousuf A. Khan[1,2,3,4,5], Kangqiang Qiu[6], Ashwin Balaji[7], Sergio Couoh-Cardel[1,2,3,4,5], Luis Esquivies[1,2,3,4,5], Richard A. Pfuetzner[1,2,3,4,5], Jiajie Diao[6], Axel T. Brunger[1,2,3,4,5 ,*]

[1]Department of Molecular and Cellular Physiology, Stanford University, Stanford, California, United States
[2]Department of Neurology and Neurological Sciences, Stanford University, Stanford, California, United States
[3]Department of Structural Biology, Stanford University, Stanford, California, United States
[4]Department of Photon Science, Stanford University, Stanford, California, United States
[5]Howard Hughes Medical Institute, Stanford University, Stanford, California, United States
[6]Department of Cancer Biology, University of Cincinnati College of Medicine, Cincinnati, United States
[7]Department of Chemistry, Stanford University, Stanford, California, United States

[*]Correspondence: brunger@stanford.edu
[**]Correspondence: kiwhite@stanford.edu

Keywords

Membrane vesicle trafficking, AAA+ protein; neurotransmitter release; synapse; nanocluster; active zone; syntaxin; SNAP-25; NSF; ATP; hydrolysis

Abstract

Synaptic vesicles containing neurotransmitters fuse with the plasma membrane upon the arrival of an action potential at the active zone. Multiple proteins organize trans-SNARE complex assembly and priming, leading to fusion. One target membrane SNARE, syntaxin, forms nanodomains at the active zone, and another, SNAP-25, enters non-fusogenic complexes with it. Here, we reveal mechanistic details of AAA+ protein NSF (N-ethylmaleimide sensitive factor) and SNAP (soluble NSF attachment protein) action before fusion. We show that syntaxin clusters are conserved, that NSF colocalizes with them, and characterize SNARE populations that may exist within or near them using cryo-EM. Supercomplexes of NSF, α-SNAP, and either a syntaxin tetramer or one of two binary complexes of syntaxin—SNAP-25 reveal atomic details of SNARE processing and show how sequential ATP hydrolysis drives disassembly. These results suggest a functional role for syntaxin clusters as reservoirs and a corresponding role for NSF in syntaxin liberation and SNARE protein quality control preceding fusion.

39 # Introduction

40 The membrane-anchored SNARE (soluble N-ethylmaleimide-sensitive factor acceptor protein
41 receptor) proteins provide the energy to drive membrane fusion in various cellular contexts, such
42 as intracellular trafficking and exocytosis. One critical exocytic process is synaptic transmission,
43 in which a synaptic vesicle fuses with the presynaptic plasma membrane in the active zone of a
44 neuron to release neurotransmitter molecules into the synaptic cleft in response to the arrival of
45 Ca^{2+} in the presynapse. While many proteins precisely act in concert to ensure synchronized and
46 efficient Ca^{2+}-triggered fusion[1–5], this process is fundamentally mediated by the "zippering" of
47 four SNARE motifs typically contributed by three to four SNARE proteins in the neuronal
48 context—syntaxin-1a and SNAP-25 on the target plasma membrane (*t*-SNAREs), and
49 synaptobrevin-2 on the vesicle (*v*-SNARE)—which come together to form a highly stable
50 parallel four-helix bundle during Ca^{2+}-triggered membrane fusion. This *cis*-SNARE complex is
51 then disassembled in an ATP-dependent manner by the AAA+ protein NSF in concert with the
52 adaptor SNAP proteins[6,7].

53 While the molecular mechanisms of this core fusion cycle and the accessory proteins required to
54 ensure Ca^{2+}-dependent neurotransmitter release have been extensively studied[4], the organization
55 of the various components in the crowded cellular milieu remains uncertain. Numerous studies
56 suggest nanoscale organization within the presynaptic active zone, where proteins and lipids[8–11]
57 such as cholesterol and PIP_2 colocalize or even phase separate into discrete clusters with
58 implications for organization within the active zone and even across the synapse[12].

59 The SNARE protein syntaxin shows such an organization[11,13]. Syntaxin is conserved from yeast
60 to mammals[14,15]; it comprises a short C-terminal transmembrane domain, a SNARE domain, and

61 an N-terminal Habc domain [16,17]. In the neuronal context, the majority (~ 67%) of syntaxin
62 molecules form nanodomains of non-uniform density[13,18], often near the active zone[8,13,18–21], and
63 these nanodomains frequently overlap with other essential active zone proteins and even docked
64 granules[11,19,20,22–25]. Morphologically, they are dense, around 50–60 nm in diameter, and harbor
65 as many as 70 syntaxin molecules each[13,18,19,22,26]. Increased presynaptic activity drives a
66 decrease in syntaxin cluster size[27]. These clusters depend on the syntaxin SNARE domain (H3),
67 which drives oligomerization[28].

68 Despite extensive study, the functional purpose of these clusters has remained unclear. Moreover,
69 NSF, α-SNAP, and syntaxin appear to interact *in vitro*[29], and α-SNAP associates with liposomes
70 presenting reconstituted full-length syntaxin[30]. Binary (syntaxin—SNAP-25) complexes of
71 different stoichiometries may also form [31–37], and NSF disassembles these complexes *in*
72 *vitro*[31,38–40]. Furthermore, continuous ATP hydrolysis by NSF on plasma-membrane mimicking
73 vesicles with reconstituted syntaxin and SNAP-25 produces a primed state for the most efficient
74 and synchronous synaptic vesicle fusion[3]. These observations support a critical role for NSF not
75 only in recycling SNARE proteins following fusion, but also in regulating the pool of fusogenic
76 syntaxin available to enter the vesicle fusion cycle.

77 Here, we show that spatially organized nanodomains of syntaxin may serve as conserved
78 molecular protein stores, where NSF likely disassembles syntaxin homo- and hetero-oligomers.
79 Thus, NSF may act as a quality control factor to disassemble off-pathway binary complexes of
80 syntaxin and SNAP-25—a prerequisite for synaptic vesicle priming and fusion. We also describe
81 the molecular disassembly mechanism and present a sequential ATP hydrolysis mechanism by
82 which NSF couples γ-phosphate release to SNARE substrate remodeling, with broad
83 implications for the AAA+ protein family.

84 # Results

85 ## Syntaxin nanodomains are conserved hotspots of NSF activity

86 First, we hypothesized that NSF is enriched at syntaxin clusters in the active zone, where it could
87 act to liberate fusogenic syntaxin molecules. To test this, we monitored the colocalization of
88 syntaxin and NSF in PC12 cells, a model system for neuronal secretion, using structured
89 illumination microscopy (SIM). All cells were transfected with syntaxin-GFP and as well NSF
90 with either a short C-terminal linker followed by mScarlet-I (NSF-mScarlet-I; Fig. 1A), a mutant
91 form of NSF (NSF(ΔN)-mScarlet-I; Fig. 1B), or mScarlet-I alone (Fig. 1C), or several
92 catalytically impaired mutants (Supplementary Fig. 1A). NSF-mScarlet-I is hexameric and,
93 together with α-SNAP, retains the capacity to bind and disassemble the ternary SNARE complex
94 (Supplementary Fig. 2A). Clear, punctate co-clustering between NSF and syntaxin is visually
95 apparent upon inspection of the micrographs (Fig. 1A–C); Pearson's colocalization coefficient
96 (PCC) was calculated between the green and red channels to quantitate this (Fig. 1D, Methods).
97 Cells transfected with both syntaxin-GFP and NSF-mScarlet-I showed significant and
98 reproducible syntaxin-GFP—NSF-mScarlet-I colocalization (Fig. 1A, PCC = 60% ± 2%; $p <$
99 0.001 vs. mScarlet-I only;), suggesting an interaction between NSF and syntaxin molecules
100 within the nanodomains. As a control, mScarlet-I alone did not colocalize with syntaxin, showing
101 a nearly three-fold reduction in colocalization (Fig 1C; PCC = 22% ± 2%). To verify that
102 colocalization is consistent with the binding mode of NSF, in which NSF N-domains engage
103 multiple α-SNAPs, which in turn coat the SNARE complex[6,40,41], we examined colocalization of
104 GFP-syntaxin with a mutant form of NSF with the N-domain required for α-SNAP binding—and
105 thus SNARE complex binding—removed (NSF(ΔN)-mScarlet-I)[42]. As expected, this reduced
106 colocalization to a level nearly indistinguishable from the mScarlet-I control (Fig. 1B, PCC =

107 28% ± 3%; $p = 0.1776$ vs. mScarlet-I only). Two previously characterized[43] point mutations to
108 the D2 domain also disrupted colocalization between syntaxin and NSF (Supplementary Fig.
109 1A–B). These colocalization studies suggest that NSF is associated with some clustered,
110 multimeric species involving syntaxin molecules *in vivo*, and that the interaction is dependent
111 upon the recognition of a left-handed, four-helix SNARE complex. While these results showed
112 clustering of syntaxin in the context of synaptic transmission, we found that clustering also
113 occurs in the case of the conserved syntaxin homolog in yeast, Sso1p, as well (Fig. 1F,
114 Supplementary Fig. 1C). During cell division, the mother cell transfers plasma membrane and
115 cargo to the budding daughter cell via secretory vesicles, and tethering and fusion take place
116 across daughter cell plasma membrane[44]; we observe Sso1p clusters enriched throughout the
117 budding cell in areas likely undergoing active fusion.

118 Discovery of a syntaxin tetramer complex with NSF—α-SNAP

119 To gain insight into the contents of the syntaxin nanodomains as well as the molecular basis of
120 the interaction between NSF and syntaxin, we purified the complex consisting of NSF, α-SNAP,
121 and soluble syntaxin (residues 2–253, transmembrane region omitted) by mixing the individual
122 purified proteins and performing size exclusion chromatography (SEC), Supplementary Fig. 3A).
123 We note that soluble syntaxin exists as a mixture of monomeric and oligomeric species[36]. We
124 then performed cryo-EM single-particle analysis (SPA) of this complex. Following 3D
125 classification, 5% of the particles formed a class with an overall resolution of 3.75 Å, revealing a
126 complex (referred to as sx20S) between hexameric NSF, four α-SNAP molecules, and a parallel
127 four-helix bundle of syntaxin H3 SNARE domains (sx20S; Fig. 2A, Supplementary Fig. 4,
128 Supplementary Tables 1–2, Supplementary Discussion). The remaining particles showed no
129 evidence of SNARE substrate. The finding of a syntaxin tetramer is consistent with crosslinking

130 mass spectrometry analysis of purified soluble syntaxin[36], and corroborates the specificity of the
131 system for parallel, left-handed, four-helix SNARE bundles as no other species identified by
132 mass spectrometry were found in complex with NSF and α-SNAP. The sx20S complex thus
133 further supports the notion that NSF and α-SNAP recognize parallel, four-helix SNARE
134 complexes of variable composition[6,7].

135 Similar to structures of hexameric NSF and α-SNAP bound to the neuronal ternary SNARE
136 complex (referred to as 20S complex) under non-hydrolyzing conditions[6,41], the sx20S complex
137 forms a three-tiered architecture (Fig. 2A). NSF comprises three structured domains connected
138 by flexible linkers—the adaptor N-domain followed by the D1 and D2 AAA+ domains. Six NSF
139 protomers come together to form the active form of the enzyme, a homo-hexamer. In the top tier,
140 or spire, the NSF hexamer's multiple N domains bind four α-SNAP molecules and a tetramer of
141 syntaxin H3 SNARE domains. This spire structure positions the N-terminal end of the syntaxin
142 tetramer near the pore of the hexameric D1 ATPase ring of NSF; this middle tier is responsible
143 for ATP hydrolysis and SNARE complex disassembly. The bottom tier consists of the non-
144 hydrolytic NSF D2 ATPase ring responsible for the oligomerization of the complex. We note
145 weak, poorly defined density on the outside of the D2 pore, suggestive of a highly mobile Habc
146 domain; this is consistent with observations of the H_{abc} domain in the yeast 20S complex of
147 Sec17, Sec18, and the yeast SNARE complex (including the syntaxin-1a homolog Sso1p), in
148 which the Sso1p Habc domain is found outside of the D2 pore, packed against the surface of the
149 ring[45]. Presumably, the remaining Habc domains extend outwards from the space between the
150 spire and the D1 ring, although they are not resolved in our structures of the neuronal 20S
151 complex.

152 The spire structure appears dynamic and rocks about relative to the D1 pore, but three of the six
153 N domains are relatively well-ordered and engaged with the α-SNAP—syntaxin sub-complex.
154 The D1 ring is asymmetric and split; protomers A–F are defined from the bottom of the split to
155 the top. All six D1 domains are ordered and engage the N-terminal linker preceding the H3
156 domain of one of the four syntaxin molecules via conserved pore loops, which position Y294
157 such that it intercalates between every other syntaxin substrate side chain passing through the
158 pore (Fig. 2B). The nucleotide states of the NSF ATPase domains are consistent with a pre-
159 hydrolysis conformation; D1 protomer A is ADP bound, while D1 protomers B–F are ATP bound
160 with no evidence for divalent cation as expected (Supplementary Table 2). All D2 protomers are
161 ATP bound and lack divalent cation.

162 While the spire in the complete sx20S complex reconstruction was ordered enough to distinguish
163 the various components, continuous disorder limited the local resolution of the spire
164 reconstruction. To overcome this, we performed signal subtraction to remove the D1 and D2
165 rings, followed by local alignment of the α-SNAP—syntaxin sub-complex structure alone
166 (Supplementary Fig. 4, Methods). This approach improved the resolution of the reconstruction of
167 the α-SNAP—syntaxin sub-complex to 4.25 Å, revealing a parallel, four-helix bundle of
168 syntaxin SNARE motifs with a density of sufficient quality to assign characteristic side chains
169 (Fig. 2C). All four helices are aligned in the same register, with a unique hydrophobic layer (-3
170 layer) composed of four F216 side chains present; remarkably, all fit within the core of the
171 bundle (Fig. 2D, Fig. 5A) and induce little overall deformation of the individual H3 domains
172 (Fig. 5B–D, bottom row). The parallel syntaxin tetramer bundle observed in our structure would
173 allow membrane incorporation of the C-terminal transmembrane domains of all four syntaxin
174 molecules (Fig. 2A).

175 To determine whether NSF and α-SNAP act to disassemble the syntaxin tetramer, we devised an
176 *in vitro*, gel-based disassembly assay (Supplementary Fig. 2B–C). Wild-type NSF, α-SNAP, and
177 soluble syntaxin (residues 2–253) were purified independently, mixed in the absence of Mg^{2+}
178 (*i.e.*, non-hydrolyzing conditions), and the sx20S complex was purified. The subsequent addition
179 of Mg^{2+} to the purified complex resulted in a significant loss of α-SNAP—syntaxin following
180 filtration relative to the non-hydrolyzing control, consistent with the disassembly of the syntaxin
181 tetramer and concurrent disassociation of α-SNAP (Supplementary Fig. 2C, 21 ± 1% loss). This
182 activity is also shown in the context of the Munc18 capture assay described below (Fig. 1E).

183 NSF-catalyzed disassembly of the tetrameric syntaxin SNARE complex 184 is required for efficient syntaxin capture by Munc18

185 NSF and α-SNAP constantly disassemble SNARE complexes at the synapse, and individual
186 syntaxin molecules can then be captured by Munc18 for efficient priming, and, ultimately, for
187 fusion to occur[3,46,47]. The capture of free syntaxin molecules, either from clusters or otherwise,
188 accompanies the formation of "on-granule" clusters of syntaxin—Munc18 complex[20,22,25], with
189 implications for animal behavior[48]. Our co-localization results (Fig. 1A–D) suggest that syntaxin
190 is at least partially sequestered in stable SNARE complexes that are a substrate for NSF. This
191 notion is further supported by the finding that α-SNAP must be present for NSF colocalization to
192 occur, as inferred from the co-localization experiments comparing NSF with and without the N-
193 domain of NSF, the deletion of which precludes α-SNAP binding (Fig. 1A–B). Finally, we note
194 that α-SNAP itself inhibits fusion by competing with Munc18 to bind syntaxin[30].

195 Having shown that NSF and α-SNAP disassemble the tetrameric syntaxin SNARE complex
196 (Supplementary Fig. 2B–C), we next performed a related experiment to test the hypothesis that

197 disassembly precedes Munc18 capture by monitoring the formation of the syntaxin—Munc18
198 complex. Again, wild-type NSF, α-SNAP, and soluble syntaxin (residues 2–253) were purified
199 independently, mixed in the absence of Mg^{2+} (*i.e.*, non-hydrolyzing conditions), and the sx20S
200 complex was purified. The pool was split in half, and Munc18 was then added to each in excess,
201 followed by the addition of either EDTA (non-hydrolyzing control) or Mg^{2+} (hydrolyzing
202 conditions) to initiate the disassembly reaction. Following incubation at room temperature for 10
203 min, size-exclusion chromatography (Fig. 1E) and SDS-PAGE (Supplementary Fig. 2D–E) were
204 performed to assess syntaxin oligomer disassembly and formation of the syntaxin—Munc18
205 complex[30].

206 Under non-hydrolyzing conditions, a supercomplex of sx20S—Munc18 formed, with some
207 syntaxin captured by Munc18. Strikingly, the addition of Mg^{2+} triggered nearly complete
208 disassembly of the tetrameric syntaxin SNARE complex, leaving free NSF, a 2-fold enriched
209 syntaxin—Munc18 and nearly two-fold enriched free α-SNAP as determined by integrated area
210 (Fig 1E). Together, these results support the notion that NSF and α-SNAP disassemble the
211 tetrameric syntaxin SNARE complex and show that complete capture by Munc18 is dependent
212 upon this disassembly process, consistent with previous observations of the inhibitory nature of
213 α-SNAP. The finding of a sx20S—Munc18 complex is not surprising, as the N-termini of the
214 syntaxin molecules remain accessible, enabling a weak syntaxin—Munc18 interaction[49].

215 Structure of a 2:1 syntaxin—SNAP-25 complex with NSF—α-SNAP

216 In addition to the syntaxin homo-tetramer, hetero-oligomers with SNAP-25 are expected to be
217 present near or even within syntaxin nanodomains. Indeed, SNAP-25 forms distinct clusters near
218 syntaxin clusters in neurons[19,22,24] and readily forms binary complexes with syntaxin *in vitro*[31–

219 [35,50,51]. Although SNAP-25 is required for fusion, assembly of a fusogenic ternary *trans*-SNARE
220 complex likely proceeds first through a syntaxin—synaptobrevin intermediate templated by
221 Munc18-1, also found near syntaxin clusters[20,24,25], and by Munc13-1[31,46,52]. Disassembly of the
222 binary complex is critical, as genetic deletion of NSF is lethal[53]. However, an NSF mutation that
223 differentially blocks ternary, but not binary, SNARE complex disassembly causes only
224 intermediate sensorineural defects[38]. Thus, NSF and α-SNAP likely disassemble binary
225 complexes of syntaxin and SNAP-25 *in vivo* to set the stage for the action of Munc18 and
226 Munc13, ultimately resulting in synchronous and efficient Ca^{2+}-triggered fusion[3,31,32,52].

227 To gain insight into the structural nature of binary complex formation and disassembly by NSF,
228 we prepared a complex of NSF, α-SNAP, and the binary *t*-SNARE complex (21bin20S)
229 composed of full-length soluble SNAP-25 and soluble syntaxin-1a (1–267) in the absence of
230 divalent cation (*i.e.*, non-hydrolyzing conditions) and performed single-particle cryo-EM
231 (Supplementary Tables 1–2, Supplementary Fig. 3B, Supplementary Figs. 5–6). First, models of
232 the NSF D1 and D2 domains with substrate bound in the D1 pore were built into two high-
233 resolution (2.88 Å, 2.92 Å) classes from a single dataset, differing only in the state of F protomer
234 engagement with substrate (Supplementary Fig. 5). Next, the dataset from which they were
235 derived was combined with two additional datasets to enable the 3D reconstruction of weakly
236 populated states with ordered density for the α-SNAP—SNARE spire (Supplementary Fig. 6).
237 Classes with evidence of NSF D1 domains engaging ordered α-SNAP—SNARE sub-complexes
238 were carried forward; eight 21bin20S models were built into reconstructions ranging from 3.39–
239 4.01 Å in resolution, differing mainly in the orientation of N domains and a sub-complex of three
240 α-SNAP molecules and four SNARE motifs relative to the D1 ATPase ring (Fig. 6A). All classes
241 revealed substrate-bound NSF without Mg^{2+} needed for ATP hydrolysis and disassembly

242 (Supplementary Table 2), and share the same overall architecture, with a spire composed of NSF
243 N-domains and the α-SNAP—SNARE subcomplex on top, the NSF D1 ring in the middle tier,
244 and the NSF D2 ring forming the bottom tier (Fig. 3A). In all cases, the NSF D1 ATPase ring
245 engages SNARE substrate, with one syntaxin molecule bound to the D1 ring pore in most
246 structures (Fig. 3B, Supplementary Table 2).

247 Like the sx20S complex, continuous variability of the α-SNAP—SNARE subcomplex was
248 present in the 21bin20S reconstructions. We again performed signal subtraction and local
249 alignment on α-SNAP—SNARE sub-complexes from all five classes with ordered spire
250 structures (Supplementary Fig. 6; see Methods). This procedure produced a single α-SNAP—
251 SNARE sub-complex reconstruction with an overall resolution of 3.74 Å (Fig. 3C), sufficient to
252 assign characteristic side chains, identify the SNAREs forming the complex and their
253 directionality (Fig. 3D, Fig. 5A). A model composed of the ternary neuronal SNARE complex[54]
254 with synaptobrevin removed was docked into the density, preserving a distinctive kink in the
255 peptide linker leading into the SN2 SNARE motif of SNAP-25. In place of synaptobrevin, a
256 second syntaxin molecule was placed to complete the four-helix bundle with little deviation from
257 its usual backbone configuration of the ternary complex (Fig. 5B). As such, the stoichiometry of
258 the syntaxin—SNAP-25 complex observed is 2:1, the dominant species in solution[33,36,50,51,55].
259 Sidechains comprising essential layers repack within the core of the complex (Fig. 3D) compared
260 to the ternary SNARE complex. For example, the ionic central layer (0 layer) is reorganized;
261 Arg56 of synaptobrevin is replaced with a second Gln226 from the additional syntaxin molecule,
262 which adopts an extended rotamer to mimic the arginine it replaces. The SNAP-25 linker, which
263 joins the two SNARE motifs, is largely disordered but blocks binding by a fourth α-SNAP
264 molecule, as observed for the neuronal SNARE complex[6].

265 Docking the 2:1 binary complex structure back into the seven individual 21bin20S
266 reconstructions reveals an apparent preference for syntaxin, with six of eight reconstructions
267 featuring the N-terminus of syntaxin H3 bound within the pore of the D1 ring (Fig. 3B). As in the
268 case of the 20S with ternary SNARE complex, this observation is consistent with previous work,
269 in which disassembly was not contingent on specific SNARE N-terminus identity[6,40]. Taken
270 together, we observe that the NSF D1 ring can bind to at least two different SNAREs, syntaxin,
271 and SNAP-25, in various configurations.

272 Structure of a 2:2 syntaxin—SNAP-25 complex with NSF—α-SNAP

273 To gain insight into the disassembly of the binary SNARE complex, we repeated the binary 20S
274 preparation but added Mg^{2+} and an ATP regeneration system[56] (*i.e.*, hydrolyzing conditions) to
275 the purified complex ~1 min before vitrification for single particle cryo-EM (Supplementary
276 Tables 1–2, Supplementary Fig. 3C, Supplementary Fig. 7). The addition of the regeneration
277 system more closely mimics the metabolic state of the cell, and it allows multiple cycles of
278 SNARE disassembly and reassembly to proceed as observed under far more dilute conditions[32].
279 Following 3D classification, 41% of particles formed a complete complex, all of which have
280 ordered α-SNAP—SNARE spire density and differ largely by spire pose (Fig. 6A). Interestingly,
281 classes with poorly defined SNARE substrate, as observed under the non-hydrolyzing condition,
282 were no longer observed. The remaining 59% of particles were SNARE-substrate free and
283 grouped into three classes with split D1 and D2 rings; presumably, this is a post-disassembly,
284 substrate-released state, and it is not observed under non-hydrolyzing conditions.

285 Substrate-bound reconstructions reveal a flattened D1 ring in closer proximity to the D2 ring and
286 a strikingly different α-SNAP—SNARE spire structure than observed in the 21bin20S complex

287 under non-hydrolyzing conditions (Fig. 4A, Supplementary Fig. 8A). Again, syntaxin is bound
288 within the pore of the D1 ring (Fig. 4B, Supplementary Table 2). We observed a nearly
289 symmetric α-SNAP—SNARE subcomplex comprising four α-SNAP molecules coating a four-
290 helix bundle. Even without further processing, this structure was recognizable as a 2:2
291 syntaxin—SNAP-25 sub-complex formed by two syntaxin H3 SNARE domains and two SNAP-
292 25 SN1 SNARE domains; this binary 2:2 configuration was previously observed in crystal
293 structures of syntaxin-1 H3 and SNAP-25 SN1 domains[34] and was unexpected as we prepared
294 the complex with full-length proteins, implying that two independent SNAP-25 molecules
295 contribute their SN1 SNARE domains to this complex. Presumably, disassembly of the binary
296 2:1 complex (Fig. 3C) had occurred and was followed by reassembly to form the 2:2 binary
297 complex (Fig. 4C) before vitrification.

298 To improve the resolution of the spire reconstruction, signal subtraction, and local alignment
299 were performed as before (Supplementary Fig. 7). This approach improved the reconstruction of
300 the spire proteins to 4.22 Å, enabling docking of a crystal structure of the 2:2 syntaxin—SNAP-
301 25 SN1 complex[34] into the density (Fig. 4C), which was of sufficient quality to assign
302 characteristic side chains, to identify the SNARE domains and their directionality (Fig. 4D, Fig.
303 5A). The 2:2 binary complex was fit back into the full reconstructions, enabling modeling of the
304 full 22bin20S. Furthermore, we were able to reproduce this result by reconstituting the complex
305 with only the SNARE domains of syntaxin and SNAP-25 under non-hydrolyzing conditions
306 (min22bin20S, Supplementary Fig. 9A–D), yielding the same spire configuration but to a higher
307 resolution of 3.86 Å following local reconstruction (Supplementary Fig. 9E, Fig. 5A). This
308 reconstruction also reveals the interface between an N-domain of NSF and an α-SNAP molecule

309 in detail; the interface is characterized by a core hydrophobic interaction surrounded by charge
310 complementation (Supplementary Fig. 9F).

311 Insights into SNARE substrate engagement and processing by NSF

312 Hydrolysis by NSF is required for efficient priming and, ultimately, fusion. Collectively, we
313 obtained many datasets with NSF, α-SNAP, and several SNARE substrates under non-
314 hydrolyzing and hydrolyzing conditions (Supplementary Tables 1–2), presenting an opportunity
315 to investigate the molecular mechanism of SNARE substrate processing and chemomechanical
316 energy transduction in NSF. Together, the resulting high-resolution structures derived from the
317 different classes from these datasets capture the hydrolysis cycle of NSF and reveal important
318 details about its reaction coordinate.

319 For datasets with particles collected under non-hydrolyzing conditions, NSF is found in two
320 general conformations, primarily differentiated by their F protomer state (Fig. 7A, left column).
321 Two high-resolution 21bin20S classes from the 2:1 binary SNARE complex dataset reveal large-
322 scale conformational displacement connected to D1 F promoter nucleotide state and SNARE
323 substrate engagement. The first class is ATP-bound and fully SNARE substrate-engaged, while
324 the second has a nucleotide-free and SNARE substrate-disengaged F protomer (Fig 5A, left,
325 bottom, and top, respectively; Supplementary Fig. 5). The engagement of F at the top of the ring
326 accompanies a relaxation of A into the split. Otherwise, the classes are nearly identical;
327 protomers B–E D1 domains also bind ATP, while protomer A, at the bottom of the D1 split, is
328 ADP-bound in both cases. Comparison of the two classes reveals limited differences outside of
329 the protomers A and F positions, as the change in protomer F position allows additional
330 relaxation of protomer A into the split.

331 In contrast to the non-hydrolyzing datasets, particles in the hydrolyzing dataset fall into two
332 categories—substrate-bound 22bin20S (Fig. 7A, middle column) or substrate-free NSF (post-
333 hydrolysis; Fig. 7A, right column), of which there are ten and three classes, respectively
334 (Supplementary Table 2, Supplementary Fig. 7). The particles show a population shift towards a
335 flatter D1 ring that is closer to D2 relative to the non-hydrolyzing class, particularly in the case
336 of the SNARE-substrate free classes, which also show an expanded pore (Supplementary Fig.
337 8A–B). Most strikingly, no SNARE substrate-bound classes show an F protomer as fully
338 engaged as those in non-hydrolyzing classes; in all but one class, F is ADP bound, SNARE
339 substrate disengaged, and sits between engaged A and E protomers. However, a subclass with an
340 ATP-bound F protomer was found using a subdivision of a large class with 3D Variability
341 Analysis[57] (3DVA; Supplementary Fig. 10C–D) for which the interprotomer interface with the
342 neighboring D1 protomer E is nearly—but not completely—formed. Critically, the pore loop
343 approaches the substrate-engaged state found in the non-hydrolyzing classes; together, this
344 reveals a trajectory of protomer A dissociation, nucleotide release and rebinding, and, finally,
345 SNARE substrate rebinding (Fig. 7D). Furthermore, in classes with ordered syntaxin substrate,
346 the unstructured region of syntaxin N-terminal to the H3 domain is engaged by the D1 pore loops
347 around eight residues further into the primary sequence under hydrolyzing conditions (Fig. 6B).

348 Sequential hydrolysis by NSF drives conformational cycling

349 As noted above, the nucleotide states of the D1 protomers help explain the pattern of engagement
350 with the SNARE substrate (Fig. 7A–C, Supplementary Table 2). How does nucleotide hydrolysis
351 drive this process? Unlike the non-hydrolyzing 21bin20S reconstructions, hydrolyzing 22bin20S
352 reconstructions are only ATP-bound in protomer E, consistent with a sequential hydrolysis
353 mechanism (Fig. 7A, middle column). Except for the rebinding F protomer described above, all

354 other D1 protomers are ADP bound with variability in the presence of Mg^{2+} and inorganic
355 phosphate (P_i); in most cases, protomers C and D have ADP•P_i and Mg^{2+}, protomer B is ADP-
356 bound, and protomer A is typically ADP-bound only. Finally, substrate-free classes are always
357 ADP bound, even in protomer E; they are flat, have some N-domains packed between the D1 and
358 D2 rings, and are characterized by a split in both the D1 and D2 rings between protomers A and
359 F (Fig. 7A, right column); this is consistent with a SNARE substrate side-loading mechanism
360 proposed for the NSF ortholog in yeast, Sec18[45]. In both hydrolyzing and non-hydrolyzing
361 datasets, all D2 domains are ATP-bound, with Mg^{2+} present in the hydrolyzing condition.
362 Together, these classes represent key steps in the hydrolysis cycle, revealing the binding of Mg^{2+},
363 hydrolysis of ATP to ADP•P_i at protomer E, and subsequent P_i release down-ring; these states are
364 accompanied by a conformational change in the Walker A, Walker B, and Sensor 1 active site
365 residues in *cis* and the arginine fingers of the down-ring protomer in *trans* (Fig. 7B), and are
366 connected in turn to larger scale conformational change within the D1 domain (Fig. 7C).
367 Critically, P_i release following hydrolysis leads to arginine finger disengagement (Fig. 7B, right
368 two panels) and subsequent relaxation and solvation of the interprotomer interface, enabling the
369 protomer A transition to protomer F and subsequent substrate rebinding.

370 What triggers hydrolysis at E, and what conformational changes follow? While hydrolysis could
371 proceed spontaneously, this would be inefficient in the absence of an ATP-bound protomer F up-
372 ring to capture accompanying substrate translocation. We hypothesized that some allosteric
373 mechanism likely regulates this process. To identify such a mechanism in an unbiased manner,
374 we performed principal components analysis (PCA) of Cα coordinates of 132 D1 protomers
375 across all datasets followed by hierarchical density-based clustering (HDBSCAN) in high-
376 dimensional space, revealing the conformational cycling of the NSF D1 protomers in a low-

377 dimensional coordinate as well as a corresponding allosteric mechanism for modulating
378 hydrolysis by protomers E (Figs. 8–9).

379 Overall, we find protomers divided into five interpretable clusters connected to ATP hydrolysis,
380 P_i release, and protomer cycling at the D1 split during SNARE disengagement, nucleotide
381 rebinding, and SNARE re-engagement (Fig. 8A). Here, we focus on the unique features of the
382 protomers E under hydrolyzing conditions in two dimensions of the 11-dimensional latent space,
383 where they cluster far from other protomers (Fig. 8A, transition 1). As noted above, protomers E
384 are the only ATP-Mg^{2+} bound D1 protomers under hydrolyzing conditions (Fig. 8B), and they are
385 uniquely characterized by an extreme large-small subdomain angle (Fig. 8C, Supplementary Fig.
386 8). Examination of PCA and clustering results reveal conformational states unique to these
387 protomers (Supplementary Fig. 10A, Fig. 8), notably a discrete Walker A (α_3) helix position
388 ("down" state) relative to the rest of the D1 large subdomain that uniquely positions the
389 nucleotide near two key catalytic residues (Sensor I, N374 and Arginine finger 2, R388; Fig. 8E
390 left, Fig. 9), a unique conformation of a highly conserved[58] segment of the N-D1 linker
391 connected to N-domain engagement ("up A" state, Fig. 8E, middle), and the absence of a fully
392 engaged "latch loop" (residues 457–467) contributed by the up-ring protomer F in *trans*
393 ("intermediate A" state; Fig. 8E, right). All three of these features appear structurally coupled
394 (Supplementary Fig. 10B) and comprise an allosteric integration mechanism by which the
395 position of nucleotide in the active site is modulated at a distance by both N-domain engagement
396 to SNARE substrate via the N-D1 linker conformation and by the presence of an up-ring
397 protomer F via latch loop engagement. This modulation in turn influences the distance between
398 key catalytic active site residues and nucleotide (Fig. 9).

399 To test the importance of the latch loop interaction in *trans*, a mutant form of NSF was generated
400 in which a portion of the latch loop (residues 460–466) is replaced with a short glycine-serine
401 linker (SGS). An NSF activity assay based on fluorescence dequenching (see Methods) shows a
402 highly significant, ~72% reduction in the rate of SNARE complex disassembly ($p = 0.0005$; Fig.
403 8D). On the other hand, the functional importance of the N-D1 linker has already been
404 established. A mutation to NSF in the most conserved region N-D1 linker, I209N, has a direct
405 behavioral effect in zebrafish; NSF(I209N) is defective in the disassembly of ternary SNARE
406 complexes but not binary SNARE complexes, explaining this phenotype[38,58]. This isoleucine side
407 chain directly contacts the engaged latch loop and is adjacent to S207, a putative phosphorylation
408 site[59], further raising the possibility of post-translational modification in regulating NSF
409 activity[60]. Together, these observations support an allosteric mechanism critical in modulating
410 NSF function.

411 Discussion

412 Using structural and biophysical studies, we have discovered a key organizational principle at the
413 active zone in the presynapse that likely involves the remodeling of syntaxin clusters. Synaptic
414 vesicle fusion and neurotransmitter release are among the most central processes of synaptic
415 transmission, and understanding the organization and the molecular mechanisms of these
416 processes in the cellular context is essential. Our work helps to answer a key unanswered
417 question—what is the purpose of phase-separated syntaxin at the presynapse?

418 Our observation of NSF colocalization to syntaxin clusters *in vivo*, coupled with direct evidence
419 of disassembly of both syntaxin tetramers and syntaxin—SNAP-25 complexes, explains a
420 previously overlooked but essential aspect of the synaptic vesicle fusion cycle with broad

421 implications for membrane trafficking (Fig. 10A). While NSF is well known for its role in
422 ternary *trans*-SNARE complex disassembly following fusion, this work, combined with
423 functional studies[3,31,32,38,52], further establishes NSF as a critical factor for synaptic vesicle
424 priming before fusion. NSF is enriched at and near syntaxin clusters, which are, in turn, found at
425 the presynapse. This enrichment is highly dependent upon the presence of the NSF N-domain,
426 which binds α-SNAP (Supplementary Figure 2E–F), which in turn binds parallel, four-helix
427 SNARE complexes through a stereotyped binding interface[6,7,61]. The observation here of a
428 parallel, four-helix syntaxin-1a bundle suggests that these clusters are structured, at least in part,
429 and that NSF and α-SNAP act to disassemble the syntaxin tetramers within or on the perimeter of
430 a given cluster, increasing syntaxin mobility at the synapse[27]. Individual syntaxin molecules
431 liberated from clusters by NSF can then be captured by the SM protein Munc18 and ultimately
432 be used to assemble fusogenic *trans*-SNARE complexes.

433 However, a high local concentration of SNAP-25 is present near the syntaxin clusters as
434 well[11,24,62], so free syntaxin may also enter a non-productive binary SNARE complex with
435 SNAP-25 with a stoichiometry dependent upon local concentrations and configurations of either
436 protein. NSF disassembly of these species prior to fusion is critical *in vivo*[38]. In this work, we
437 observe binary complexes with two stoichiometries—2:1 and 2:2 binary complexes of syntaxin
438 and SNAP-25, with the latter re-forming following NSF-mediated disassembly of the former
439 under hydrolyzing conditions. The 2:1 configuration dominates in the non-hydrolyzing
440 condition—and in other *in vitro* studies[33,51]—but is derived from co-expressed proteins that were
441 extensively purified without NSF action. The 2:2 configuration is only found following NSF-
442 mediated disassembly of the 2:1 configuration. This striking observation is likely related to
443 differences in the effective concentration of syntaxin dimers preceding complex formation during

444 expression in and purification from *E. coli* versus following disassembly *in vitro*[55]. Regardless,
445 these structures are consistent with the notion that SN1 is a critical initial mediator of SNARE
446 assembly[63]. The structural plasticity of the SNARE complexes is also of note; taken together, the
447 repeated observation of a twisted, parallel, four-helix bundle with minimal backbone distortion
448 (Fig. 5) emphasizes the functional conservation latent in the SNARE domain sequences studied
449 thus far, as well as the importance of additional SNARE protein accessory domains in
450 differentiating SNARE protein function[45]. Thus far, only parallel SNARE bundles have been
451 observed the context of various 20S complexes in this work and elsewhere[6,7,32,61]. While NSF
452 and alpha-SNAP rapidly disassemble anti-parallel SNARE complexes[32], such complexes may be
453 too rare or heterogeneous to be observable by cryo-EM.

454 We note that several recent studies[20,48] also highlight the critical connection between syntaxin
455 clustering, neurotransmission, and animal behavior and emphasize the role of the protein
456 Munc18 in capturing free syntaxin from clusters for subsequent priming. Our disassembly results
457 show that syntaxin capture by Munc18 depends on its liberation from SNARE complexes (Fig.
458 1E) on the timescales of synaptic transmission. This is also consistent with previous observations
459 of increasing syntaxin mobility at the synapse with NSF action[27]. As such, a complete
460 mechanistic picture of the system involves NSF, α-SNAP, and Munc18; Munc18 can directly
461 bind any monomeric syntaxin at or near the syntaxin clusters, but it likely cannot actively
462 remove syntaxin from oligomeric complexes within the clusters, especially on the timescales of
463 synaptic transmission. Our model also suggests a mechanism for the transit of syntaxin from off-
464 pathway, Munc18-free clusters to on-granule clusters of syntaxin-1a—Munc18[20,22] and further
465 explains the inhibition of Munc18 binding of syntaxin by α-SNAP[30].

466 Regardless, NSF and α-SNAP likely disassemble both syntaxin tetramers and binary SNARE
467 complexes to maintain a fusogenic population of *t*-SNAREs[3,38], which ultimately enter the *trans*-
468 SNARE complex with the *v*-SNARE synaptobrevin-2 and set the stage for Ca^{2+}-triggered fusion
469 in cooperation with synaptotagmin and complexin[64,65]. Indeed, the energy released by SNARE
470 protein zippering during vesicle fusion can be directly traced to the hydrolysis of ATP by NSF,
471 which effectively maintains them in a high-energy state. Thus, syntaxin nanodomains could
472 effectively act as high-density storage sites for syntaxin, and NSF could tap these stores under
473 periods of high-frequency vesicle release. Modulation of NSF activity by post-translational
474 modification could thus be one way to regulate this process[38,60]. Finally, given the observation of
475 clustered Sso1p in yeast, and the high degree of structural and functional conservation between
476 NSF and Sec18[45], this seems likely to be a conserved organizing principle across fusion contexts.

477 At the atomic level, how does NSF accomplish the energy transfer needed to disassemble various
478 SNARE complexes? The structural details of the hydrolysis cycle (Fig. 7) are consistent with
479 sequential hydrolysis by the six D1 ATPase domains of NSF. Hydrolysis drives conformational
480 change, which is coupled to the application of force to one member of the SNARE complex,
481 destabilizing it and promoting disassembly over multiple hydrolysis events (Fig. 10B,
482 Supplementary Movie 1). Rather than relying on a non-physiological nucleotide state promoted
483 by chelation of divalent cations or non-hydrolyzable nucleotide analogs (*e.g.*, ATPγS), we
484 established a reaction condition more closely approximating cellular metabolism by using a
485 physiological ATP regeneration system. Our sequential hydrolysis model suggests that hydrolysis
486 proceeds around the asymmetric NSF D1 ring, occurring near the "top" of the ring at protomer E.
487 Down-ring protomers reveal evidence for a transient post-hydrolysis reaction state in which
488 ADP•P_i is generally observed before P_i release from protomers C or B and an associated

489 disruption and solvation of the interprotomer interface. This mechanism is likely conserved in
490 other members of the AAA+ family, such as p97 (Supplementary Discussion).

491 Furthermore, the continuous transition from protomer A at the bottom of the ring to protomer F
492 at the top follows ADP release and ATP rebinding (Fig. 10B, Supplementary Fig. 10D–E,
493 Supplementary Movie 1). This cycling appears coupled to the triggering of hydrolysis at
494 protomer E in a process allosterically mediated by several key structural elements (Figs. 8–9);
495 presumably, full protomer F rebinding triggers hydrolysis, likely driven by an allosteric shift
496 associated with full latch engagement with the N-D1 linker region, further formation of the
497 interprotomer interface, and mediation of the distance between nucleotide and key catalytic
498 residues such as Sensor I and the second Arginine finger (N374 and R388, respectively; Fig. 9).
499 Protomer F rebinding is also connected to the mechanism by which engagement of the SNARE
500 substrate is maintained during processing. In the absence of a completely protomer F-rebound
501 state in the hydrolyzing condition, however, we cannot distinguish between SNARE substrate
502 rebinding before or after protomer E hydrolysis; the former case (ATP in fully rebound F and E)
503 represents a classical "hand-over-hand" mechanism, while the latter case (ATP in fully rebound
504 F, ATP ADP•Pi in E), a ratchet mechanism in which F re-engages substrate during or
505 immediately following a translocation event driven by protomer E hydrolysis, locking in
506 substrate translocation[66]. The flattened D1 rings of the SNARE-substrate-free classes with
507 ADP•Pi in protomers E (Supplementary Fig. 8) are suggestive of the latter; flattening upon
508 hydrolysis at protomer E could exert a pulling force on the substrate, and translocation would
509 then take place with substrate engagement by a new protomer F and release of the old protomer
510 A. Multiple rounds of translocation are expected to ultimately lead to melting of the engaged
511 SNARE domain and subsequent disruption of the SNARE complex. These large-scale

512 conformational changes may also apply a force via the NSF N-domains, which could aid in the
513 disassembly process[6,7,61].

514 Together, our findings expand the role of NSF in synaptic transmission and the membrane fusion
515 cycle while further demonstrating its contribution as a model system for understanding energy
516 transduction and protein remodeling in AAA+ proteins. NSF acts as a mobile engine of the
517 presynapse—working together with the SNAP adaptor proteins and factors such as Munc18 to
518 convert the chemical energy latent in ATP into the physical work needed to organize, maintain,
519 and drive synaptic function through the disassembly of a variety of SNARE proteins.

520 Methods

521 **PC12 transfection and imaging**

522 The PC12 cells, generously provided by Prof. Tobias Meyer from Stanford University, were
523 cultured on glass-bottomed dishes (MatTek; P35G-1.5-14-C) and allowed to adhere for 24 hr. To
524 introduce genetic material into the cells, transfection was performed using the TurboFect™
525 Transfection Reagent (#R0532, Thermo Fisher Scientific, USA) according to the manufacturer's
526 instructions. In brief, the plasmids (NSF-GGGSGGGS-mScarlet-I in pTwist CMV Puro, 1.75
527 μg; syntaxin1a-eGFP plasmid, 0.5 μg) were combined with 6.75 μL of TurboFect in 225 μL of
528 DMEM medium (without FBS) and incubated for 20 min. The DNA-TurboFect mixtures were
529 carefully added drop-wise to the cell cultures and incubated for 6 hr. Following the incubation,
530 the cell cultures were replaced with complete culture medium. After 24 hr post-transfection, the
531 cells underwent three washes with PBS. Subsequently, the cell membranes were imaged using a
532 structured illumination Nikon N-SIM system (version AR5.11.00 64bit, Tokyo, Japan) equipped
533 with an Apochromat 100×/1.49 numerical aperture oil-immersion objective lens. Using a 488 nm

534 laser, the samples were excited to acquire green SIM images, which captured emission within the
535 500–550 nm bandwidth, specifically for GFP. Additionally, red SIM images were obtained by
536 exciting the samples with a 561 nm laser to capture emission within the 570–640 nm bandwidth,
537 corresponding to mScarlet-I. To determine the degree of colocalization between syntaxin and
538 NSF, Pearson's correlation coefficient was calculated between channels *ImageJ*[67].

539 **Yeast imaging**

540 The Sso1-GFP strain was created previously[68] and provided by the lab of Daniel Jarosz; the yeast
541 harbors a plasmid with Sso1-GFP similar to that used in the PC12 experiments, in which GFP is
542 found outside of the cell while Sso1p itself is in the plasma membrane and cytoplasm. BY4741 is
543 the parental strain; N-SWAT Sso1 GFP is the protein, and **MATa his3Δ1 leu2Δ0 met15Δ0**
544 **ura3Δ0** is the genotype. Expression was carried out using the native yeast promoter NOP1.
545 Super-resolution microscopy of *S. cerevisiae* expressing Sso1-GFP was performed using
546 structured illumination microscopy (SIM) on the OMX-Blaze system (Applied Precision,
547 Issaquah, WA). Glass-bottom dishes (1.5H, Cellvis) were pretreated with 0.01% poly-l-lysine by
548 adding 600–1000 µL to the center and incubated overnight. Following incubation, the dishes
549 were washed with deionized water to remove excess poly-l-lysine. Yeast cultures were grown
550 overnight, washed twice with phosphate-buffered saline (PBS), and resuspended to an optical
551 density (OD) of 0.4. A 10–20 µL volume of the yeast suspension was deposited onto the treated
552 dishes, followed by the addition of Diamond Antifade (Thermo Fisher Scientific) to prevent
553 photobleaching during imaging. The glass-bottom dishes were placed in a metal holder with 1–2
554 drops of immersion oil (refractive index 1.512) added before placement on the microscope stage.
555 SIM imaging was conducted using a laser appropriate for GFP excitation, and images were

556 captured with a 100× objective for a *z*-slice thickness of 0.125 µm, spanning a total thickness of
557 2.6 µm. Widefield images were also collected at 0.2 µm slice thickness when necessary.

558 **Protein expression and purification**

559 All NSF, the wild-type and mutant NSF-mScarlet-I, and NSF(Δ460–466) proteins were derived
560 from NSF from the Chinese hamster *C. griseus*, expressed in BL21(DE3)-RIL *E. coli*, and
561 purified as described previously[6], with final reassembly of hexameric NSF in reassembly buffer
562 (50 mM Tris pH 8.0, 150 mM NaCl, 1 mM EDTA, 1 mM ATP, and 1 mM TCEP). α-SNAP from
563 rat *R. norvegicus* was expressed in *E. coli* and purified as described previously[69]. Soluble rat
564 neuronal SNARE complex for the fluorescence-based disassembly assay (wild-type SNAP-25A,
565 syntaxin-1A 1–265, and 6×His-synaptobrevin-2 1–96) was purified by co-expression in C41 *E.*
566 *coli* and purified as described previously[69] Purified soluble rat neuronal SNARE complex was
567 fluorescently labeled with Oregon Green 488 maleimide dye as described previously[6].

568 Syntaxin-1A fragment 2-253 (Stx^{2-253}) was N-terminal His_6-tagged using the plasmid pTEV5.
569 Overexpression in *E. coli* BL21(DE3) was carried out in 8 L of auto-inducible media at 37ºC for
570 4 hr and then 30ºC overnight. Cells were collected by centrifugation; half of the pellet was
571 resuspended into 200 mL of 50 mM TRIS pH 8, 500 mM NaCl, and 10 mM imidazole and
572 supplemented with DNAse, lysozyme, 1 mM $MgCl_2$, and 2 eComplete Protease Inhibitor
573 Cocktail tablets (Roche). Cells were lysed by sonication (1 s on/3 s off, total 20 min, 55%
574 amplitude, 4ºC). Debris were removed by centrifugation at 43,000 rpm for 30 min at 4ºC using a
575 Ti45 rotor. The supernatant was then mixed with 5 mL of nickel-NTA agarose resin (Qiagen)
576 equilibrated with the lysis buffer. The suspension was gently stirred for 1 hr at 4ºC. The resin was
577 subsequently recovered by centrifugation at 4,200 rpm for 10 min at 4ºC, poured into a column,
578 and attached to an AKTA Start (Cytiva). An extensive wash was performed using 20 CV of 50

579 mM TRIS pH 8, 500 mM NaCl, and 40 mM imidazole until the 280 nm signal was stable.
580 Protein was eluted in 1 mL fractions in 50 mM TRIS pH8, 200 mM NaCl, and 400 mM
581 imidazole. Syntaxin-enriched fractions were identified by SDS-PAGE and pooled. To remove the
582 His-tag, the protein was mixed with an excess of TEV protease and dialyzed against 20 mM
583 HEPES pH 7.5, 50 mM NaCl, 1 mM DTT, overnight at 4ºC. The sample was centrifuged at
584 4,000 rpm for 10 min at 4ºC, filtered, and loaded onto a Mono-Q 5/50 column attached to an
585 AKTA Pure (Cytiva). The resin was extensively washed with 20 mM HEPES pH 7.5, 50 mM
586 NaCl, 0.2 mM EDTA until 280 nm signal was stable. Elution was performed in 120 CV over 2 hr
587 from 0.050–1 M NaCl. 2 mL fractions within the major peaks were run on SDS-PAGE, and
588 fractions containing Stx^{2-253} were concentrated using a 10 kDa cutoff centrifugal filtration device.
589 The concentrate was filtered and further purified using a Superdex Increase 75 16/60 column
590 (Cytiva) equilibrated with 20 mM TRIS pH 8, 150 mM NaCl. Fractions were run on an SDS-
591 PAGE, and fractions containing Stx^{2-253} were concentrated using a 10 kDa MWCO centrifugal
592 filtration device. A final concentration of 745 mM was determined by using the extinction
593 coefficient 5,960 M^{-1} cm^{-1}. Stx^{2-253} was aliquoted, flash frozen, and stored at -80ºC until further
594 use. An independent sample purified from the same batch of cells was analyzed on MALDI-TOF,
595 and a monomeric molecular weight of 29,208.50 g/mol was confirmed.

596 Binary neuronal SNARE complex for cryo-EM imaging studies (SNAP-25A with all cysteines
597 mutated to serine, syntaxin-1A 1–267) was purified following co-expression of SNARE proteins
598 from *E. coli* BL21 STAR (Invitrogen). Cells were grown overnight at 30°C using an auto-
599 inducing LB medium[70]. After harvesting the cells by centrifugation, the pellet was resuspended
600 in lysis buffer (50 mM NaPi pH 8.0, 300 mM NaCl, 20 mM imidazole, 0.5 mM TCEP)
601 supplemented with lysozyme, DNase I, and antiprotease tablets (Roche) and subjected to

602 sonication (3 s on, 9 s off, 60% power for 5 min, repeated 3×) and centrifugation (10,000 rpm for
603 10 min followed by 43,000 rpm for 40 min). The clarified lysate was bound to Ni-
604 NTA agarose beads (QIAGEN) equilibrated in a lysis buffer. Beads were harvested by
605 centrifugation (2200 rpm for 10 min), poured into a gravity column, and washed with lysis
606 buffer, urea buffer (50 mM NaP_i pH 8.0, 300 mM NaCl, 30 mM imidazole, 0.5 mM TCEP, 7.5 M
607 urea), and wash buffer (50 mM NaPi pH 8.0, 300 mM NaCl, 30 mM imidazole, 0.5 mM TCEP).
608 The SNARE complex was then eluted with wash buffer supplemented with an additional
609 320 mM imidazole. The fresh eluent of the Ni-NTA affinity purified SNARE complex was
610 supplemented with tobacco etch virus (TEV) protease and dialyzed against buffer A1 (50 mM
611 Tris-HCl, pH 8.0, 250 mM NaCl, 0.5mM TCEP) overnight at 4°C. After dialysis, the sample was
612 diluted to a final NaCl concentration of 50 mM using buffer A1 without NaCl, and the His-tag-
613 free complex was subjected to anion exchange chromatography (Buffer A2: 50 mM Tris-HCl, pH
614 8.0, 50 mM NaCl, 0.5 mM TCEP; Buffer B1: 50 mM Tris-HCl, pH 8.0, 500 mM NaCl, 0.5 mM
615 TCEP) using a MonoQ 4.6/100 column (Cytiva) and a linear gradient of NaCl starting at 50 mM
616 and ending at 500 mM. The peaks containing the purified complex were pooled and loaded onto
617 a Superdex 75 16/60 column to normalize NaCl concentration (50 mM Tris-HCl pH 8.0, 50 mM
618 NaCl, 0.5 mM TCEP).

619 The sx20S supercomplex was formed by mixing ATP-bound NSF, syntaxin, and α-SNAP to a
620 ratio of 1:5:30 in reassembly buffer and purifying it by size-exclusion chromatography using a
621 Superose 6 10/300 GL column; the first peak to elute was collected and concentrated to around
622 15 mg mL^{-1} for vitrification and cryo-EM imaging. The 21bin20S supercomplex was purified
623 similarly but with a 1:5:30 ratio of NSF, binary SNARE complex, and α-SNAP. In the case of

624 preparing 21bin20S supercomplex for imaging under hydrolyzing conditions, EDTA was omitted
625 from the final SEC buffer.

626 **Size exclusion chromatography (SEC)-based syntaxin disassembly and Munc18 capture**
627 **assay**

628 The sx20S complex was prepared as described in the "Protein expression and purification"
629 Methods Section without EDTA in the reassembly buffer and with a 1:50:30 ratio of ATP-bound
630 NSF, syntaxin, and α-SNAP. The NSF and α-SNAP concentrations were informed by the fraction
631 of sx20S to NSF in the cryo-EM experiment (Supplementary Fig. 4) and resulted in an increase
632 of the fraction of 20S with the tetrameric syntaxin SNARE complex relative to free NSF.
633 Following concentration to 50 mg mL^{-1} (or around 66 μM assuming full sx20S formation,
634 although the actual concentration is likely lower), the sx20S sample was split into two 35 μL
635 pools and resuspended to 500 μL in 464 μL of 43 μM Munc18, for a final concentration of 5 μM
636 sx20S (likely lower) and 40 μM Munc18. Either 1 μL of 500 mM EDTA or 1 μL of 500 mM
637 $MgCl_2$ was then added to the pool, in the latter case initiating the disassembly reaction.
638 Following incubation for 10 min at room temperature, the pools were independently subjected to
639 size exclusion chromatography using a Superdex 200 Increase 10/300 GL column (Cytiva), and
640 fractions were analyzed by SDS-PAGE. Absorbance data for each run were processed using the
641 script *elution.py*. Data parsed using *pandas*[71] and *numpy*[72], smoothed using Savitzky-Golay
642 filtering as implemented in *scipy*[73] with a window of 1000 points and a polynomial order of 2,
643 and peaks with absorbance amplitudes greater than 10 mAU, distances greater than 1 mL, and
644 prominences greater than 0.5 mL were found using *find_peaks* in *scipy.* Peaks were integrated
645 using the *trapz* function as implemented in *numpy.* Data were plotted using *matplotlib*[74].

646 **Filtration-based syntaxin disassembly assay**

647 Soluble syntaxin (2–253) and α-SNAP were mixed at concentrations of 100 μM and 150 μM,
648 respectively, in 50 mM Tris pH 8.0, 150 mM NaCl, 1 mM TCEP, and 1 mM EDTA (SEC buffer)
649 and incubated for 20 min. NSF was subsequently added to a final concentration of 2.5 μM,
650 bringing the total reaction volume to 500 μL. The mixture was then injected into a Superdex 200
651 16/60 column (Cytiva) and complex peak fractions were pooled and concentrated using a
652 100,000 MWCO filtration device. For each assay condition, 5 μg of complex was used. Two
653 experimental conditions were performed in triplicate; either EDTA or $MgCl_2$ was added to a final
654 concentration of 4 mM. Samples were incubated for 20 min at room temperature and re-
655 concentrated using 100k MWCO filters before SDS-PAGE. Re-concentration effectively de-
656 enriches liberated syntaxin and α-SNAP molecules. Densitometry was performed using
657 *ImageJ*[67], and statistical significance was established between the conditions using a two-tailed
658 Student's *t*-test.

659 **Gel-based ternary SNARE complex disassembly assay**

660 To verify that NSF activity was not hampered by the C-terminal addition of mScarlet-I, SNARE
661 complex disassembly was evaluated by gel electrophoresis. Note that the ternary neuronal
662 SNARE complex runs as a single band unless boiled in SDS buffer, or disassembled by NSF, in
663 which case the individual SNARE components are enriched as the complex band disappears.
664 NSF, NSF-mScarlet-I, α-SNAP, and the neuronal SNARE complex were dialyzed into 25 mM
665 TRIS pH 8, 150 mM NaCl, 1 mM ATP. Then, components were combined into either EDTA
666 buffer (25 mM TRIS pH 8, 2 mM ATP, 1 mM EDTA) or Mg^{2+} buffer (25 mM TRIS pH 8, 2 mM
667 ATP, 4 mM $MgCl_2$). The reaction volume was 10 μL, and contained 500 nM NSF or NSF-
668 mScarlet-I and 50 nM α-SNAP. Assays were started by adding 10 μM SNARE complex, and
669 samples were then incubated at 37ºC for 10 min in a thermocycler. 2 uL of 5×-Laemli loading

670 buffer was then added, and samples were incubated at 95ºC for 5 min. Finally, 5 µL of each
671 reaction was loaded onto an AnykD TGX gel (BioRad) and run at 200 V for 45 min. The gel was
672 stained with Coomassie R-250 (BioRad). As internal controls, all single components were diluted
673 at a similar concentration as the reactions using Mg^{2+} buffer and treated in parallel. Note that the
674 additional control marked as "SNARE complex unboiled" corresponds to the SNARE complex
675 incubated at 37ºC but not at 95ºC after adding loading buffer. For reference, monomeric NSF is
676 ~83 kDa while NSF-mScarlet-I is ~112 kDa.

677 **Fluorescence dequenching-based neuronal SNARE complex disassembly assay**

678 The details of the fluorescence dequenching assay have been previously described[6,32,38,40,41,69].
679 Fluorescence dequenching assays were carried out using a FlexStation II 384-well plate reader
680 (Molecular Devices) with a final reaction volume of 60 µL in 20 mM Tris pH 8, 100 mM NaCl, 2
681 mM ATP, and 0.5 mM TCEP. The assay plate was first prepared by adding 50 µL of 60 nM wild-
682 type or Δ460–466 mutant NSF, 2.4 µM α-SNAP, 480 nM OG-labeled neuronal SNARE complex
683 in reaction buffer to each well. Then, 10 µL of reaction buffer (as a control) or ATP hydrolysis
684 initiation buffer (reaction buffer supplemented with 24 µM $MgCl_2$) was added to appropriate
685 wells of the compound plate, and fluorescence dequenching was monitored. Excitation was
686 performed at 485 nm, and emission was monitored at 525 nm with a dichroic mirror at 515 nm.
687 First, fluorescence intensity was monitored before reaction initiation for 60 s. Then, 10 µL of
688 compound plate solution was transferred to each assay plate well (diluting all protein 5/6-fold
689 and $MgCl_2$ concentrations six-fold) and triturated, initiating the disassembly reaction. The final
690 protein concentrations following mixing were 50 nM NSF, 2.0 µM α-SNAP, and 400 nM
691 SNARE complex. The final $MgCl_2$ concentration was 4 mM. Dequenching was then monitored
692 for 30 min at 20 ºC. Linear regression over the first several minutes was performed to estimate

693 relative disassembly rates. The statistical significance of changes to disassembly rates was
694 assessed using the two-tailed Student's *t*-test.

695 **Sample vitrification for cryo-EM SPA**

696 The samples were prepared immediately before vitrification (Supplementary Fig. 3). Quantifoil
697 R1.2/1.3 200 mesh gold grids (Quantifoil Micro Tools GmbH, Germany) were cleaned with
698 chloroform, dried for several hours, and subjected to glow discharge using a PELCO easiGlow
699 Glow Discharge Cleaning System (Ted Pella) under vacuum at 15 mA for 45 s with a 15 s hold
700 time. Immediately following 21bin20S or sx20S supercomplex purification, proteins were
701 concentrated to ~15 mg mL^{-1} in 17 μL. For the hydrolyzing condition, 2 μL of 10 × ATP
702 Regeneration Solution (50 mM Tris pH 8.0, 150 mM NaCl, 1 mM ATP, 160 mM creatine
703 phosphate, and 0.3 mg/mL rabbit muscle creatine kinase (Roche)) was added, and the sample
704 was incubated on ice for 2 min; in contrast, 2 μL of reassembly buffer was added in the case of
705 non-hydrolyzing conditions. Then, for the hydrolyzing condition, 1 μL of 20 × Reaction
706 Initiation Solution (50 mM Tris pH 8.0, 150 mM NaCl, 1 mM ATP, 20 mM $MgCl_2$, 1% Nonidet
707 P-40) was added, otherwise 1 μL of 1% Nonidet P-40 was added in the case of non-hydrolyzing
708 conditions. Using a Vitrobot Mark IV (Thermo Fisher Scientific), 4 μL of a given sample was
709 applied to a grid at room temperature and 100% humidity and, blotted for 4 s with a blot force of
710 3, and subsequently plunge-frozen in liquid ethane.

711 **Cryo-EM SPA data collection**

712 Grids were imaged using a Titan Krios electron microscope (Thermo Fisher Scientific) operated
713 at 300 kV and equipped with a K3 camera (Gatan). Data collection was performed using
714 *SerialEM*[75]. All datasets were collected with a nominal magnification of 22,500× for a physical
715 pixel size of 1.096 Å and a super-resolution pixel size of 0.548 Å. The dose rate was either ~10

716 or ~20 e^-/px/s depending on whether correlated double sampling (CDS) was enabled on the K3,
717 for a total dose of around 30 $e^-/Å^2$. Nine grid holes were imaged for each stage movement using
718 the multiple record setup in *SerialEM*, with one collection per hole. At each hole, either a 2 s or 4
719 s exposure fractionated into either 40 or 80 frames was collected, depending on whether CDS
720 was enabled. Defocus values ranged from -1–-3 µm. See Table 1 for details.

721 **Cryo-EM SPA image processing**

722 All cryo-EM datasets were processed using a software pipeline consisting of *MotionCorr2*[76],
723 *CTFFIND4*[77], *RELION 3*[78,79], and *cryoSPARC*[57,80]. Early-stage processing was carried out in
724 *RELION 3*, with final 3D refinement and variability analysis carried out with *CryoSPARC*.
725 Dataset-specific processing schemes are presented in Supplementary Figs. 4–7 and
726 Supplementary Fig. 9. Generally, all processing proceeded as follows. Processing began in
727 *RELION 3*, with per-micrograph optics groups defined for a given dataset based on the nine
728 beam shift positions using the custom script *update_relion_tilt_class_og.py*. For example, the
729 hydrolyzing condition micrographs were collected in two sessions, so 18 total optics groups were
730 defined. The raw image stacks were dose-weighted and motion-corrected using the *RELION*
731 implementation of *MotionCorr2*, with seven patches along the *x* direction and five patches along
732 *y*. CTF parameters were estimated for each micrograph using *CTFFIND4* with a resolution range
733 of 3–30 Å, an FFT box size of 1024 px, and otherwise default parameters. Micrographs were
734 then selected based on maximum resolution and the CTF figure of merit.

735 Generally, an initial round of manual picking, extraction, and 2D classification were used to
736 assess data set quality and provide particles to reconstruct an initial 3D model. Good particles
737 from manual picking were then used for automated particle picking in *RELION*. Particles were
738 then extracted with a box size of 640 px, binned 8× (4.384 Å Å pixel size) to a box size of 80 px,

739 and subjected to at least one round of 2D classification to eliminate obviously bad particles.
740 Next, multiple rounds of 3D classification with a 280 Å mask diameter and a regularization
741 parameter $T = 4$ were performed over many iterations to determine the proper number of discrete
742 states in a given dataset, and to ensure that particles were classified properly. Convergence of
743 classification was monitored with a custom script, *startle.py*. Several classes slightly larger than
744 the number of discrete states were used, and classes that appeared to lie along a continuous
745 conformational coordinate were subsequently re-merged into a single class. In the case of the
746 hydrolyzing dataset, SNARE substrate-bound and SNARE substrate-free particles were split into
747 separate groups of particles, re-classified, and processed independently.

748 Following classification, particles were re-centered and re-extracted with a box size of 588 px
749 and binned 2× (1.096 Å pixel size) with a box size of 294 px. Following an initial round of 3D
750 refinement and post-processing, CTF refinement was performed. Typically, defocus,
751 astigmatism, B-factor, tilt, and trefoil were refined on a per-particle or per-micrograph basis,
752 depending on the specific class. Particles were then subjected to an additional round of 3D
753 refinement and post-processing, and optimal parameters for particle polishing were determined
754 by training on several classes, yielding different parameter sets. Particle polishing was then
755 performed with these sets, and 3D refinement and post-processing were used to assess the
756 results. Polished particles were then subjected to a final round of 3D refinement, post-processing,
757 and CTF refinement, during which anisotropic magnification was estimated. At this stage,
758 particles and 3D reconstructions were imported into *CryoSPARC* for a final round of non-
759 uniform refinement, which typically improved the quality of reconstructions.

760 In the case of one class observed under hydrolyzing conditions (c4-7-16-20-24), a large degree of
761 continuous heterogeneity was observed. 3D variability analysis (3DVA) revealed a trajectory of

762 protomer F nucleotide and rebinding, so particles in the first mode were split using a custom
763 script, *split_by_3dva.py*, as current tools to do so natively were unavailable at the time. This
764 script fits a normal distribution to the eigenvector magnitude distribution and allows slicing with
765 different cutoffs. For the 3DVA subclasses (slices O and P), particles in the ±1.5 σ tails of the
766 distribution were used for reconstruction.

767 These reconstructions were considered final for the overall 20S architecture, but further
768 processing was required to generate local reconstructions of the various α-SNAP—SNARE
769 subcomplexes. In the case of the sx20S dataset, only one class was observed with ordered spire
770 density, so local refinement was relatively simple. *CryoSPARC* signal subtraction
771 (*particle_subtract*; masks generated using *Segger* 2.5.3[81] in *Chimera* 1.15[82]) was used to remove
772 the signal from NSF N, D1, and D2 domains, leaving only the α-SNAP—syntaxin H3 SNARE
773 domain tetramer subcomplex. Local refinement (*new_local_refine*) was then performed on these
774 particles with a 40º/20 Å search extent and a custom fulcrum at the N-terminal end of the
775 SNARE bundle near the point of interaction with the F protomer of the D1 ring. The resulting
776 volumes were re-centered on the center of mass (*volume_alignment_tools*), and particle
777 alignments were updated as well (*align_3D*). Then, a final round of local refinement
778 (*new_local_refine*) was performed with the map center as the fulcrum (the default setting), a
779 smaller search extent of 10º/5 Å, and a maximum alignment resolution of 0.1º. Per-particle scales
780 were also reset, and minimization was performed over a per-particle scale. This produced the
781 final reconstruction of this subcomplex for subsequent modeling. In the case of the α-SNAP—
782 2:1 and α-SNAP—2:2 binary SNARE subcomplexes, this procedure was followed for each class
783 meeting certain criteria (number of particles, ordered spire, resolution), yielding five local
784 reconstructions for the α-SNAP—2:1 binary SNARE subcomplex and six local reconstructions

785 for the α-SNAP—2:2 binary SNARE subcomplex. In each case, these reconstructions were re-
786 centered (*volume_alignment_tools*), aligned to one another with the center of mass at the origin
787 (*align_3D)*, and a final round of local refinement was run to produce a final higher-resolution
788 reconstruction incorporating data from multiple classes. This produced the final reconstruction of
789 these subcomplexes for subsequent modeling. For more details about all data sets, see
790 Supplementary Figs. 4–7, Supplementary Fig. 9, Supplementary Tables 1–2, and Supplementary
791 Fig. 11.

792 **Model building and refinement**

793 All manual model building and refinements were carried out using *Coot*[83]. Semi-manual
794 refinement into low-resolution features was performed with *UCSF ChimeraX*[84] and the
795 *ISOLDE*[85] plugin. Automated refinement was performed using *phenix.real_space_refine*[86,87]. No
796 composite maps were used at any stage of model building or refinement.

797 First, models of the three α-SNAP—SNARE subcomplexes were built by rigid body fitting of
798 the best possible starting models into their corresponding densities using *UCSF ChimeraX*. In
799 each case, 3–4 copies of a high-quality α-SNAP model from the previous best 20S model (PDB
800 ID 6MDM[6]) were rigid body fit into the density. In the case of the syntaxin H3 domain tetramer
801 complex, four copies of the syntaxin chain from the high-resolution crystal structure (PDB ID
802 1N7S[54]) of the neuronal SNARE complex were docked into the density, with several
803 characteristic residues as fiducials. The quality of the local reconstructions of the SNARE—α-
804 SNAP spires allowed unique assignment of the identity of the SNARE domains, their
805 directionality, and register. In the case of the 2:1 binary SNARE complex, the syntaxin and
806 SNAP-25 components of the same crystal structure were docked into the density, but with the
807 SNARE domain of synaptobrevin replaced with an additional syntaxin H3 SNARE domain; key

808 side chain densities as well as a distinctive kink leading into the SNAP-25 SN2 domain guided
809 placement (Fig. 3C, Fig. 5A). In the case of the 2:2 binary SNARE complex, a previous crystal
810 structure (PDB ID 1JTH[34]) was docked into the density without modification. In all cases,
811 individual components were trimmed, or residues were added where supported by the density. A
812 round of *phenix.real_space_refine* was then performed with only rigid-body refinement enabled
813 for each component. Subsequent cycles of manual model building were performed in *Coot* and
814 *ISOLDE* followed by 1–7 macrocycles of *phenix.real_space_refine* with global minimization and
815 local grid search enabled. Ramachandran and secondary structure restraints were used
816 throughout. Note that while sequence information was included upon deposition for the full-
817 length construct used in the case of each SNARE, some regions (e.g., the syntaxin Habc domain,
818 the SNAP-25 SN2 domain in the case of the 2:2 binary SNARE complex) were not visible in the
819 reconstructions and were not modeled as a result.

820 Reference models of NSF were then built. Gold-standard models were first built into two high-
821 resolution NSF classes from a single non-hydrolyzing dataset with near-atomic resolutions using
822 the previous best model of NSF (PDB ID 6MDM[6]) as a starting model. The starting model was
823 first docked into cryo-EM density using ChimeraX. Next, a round of *phenix.real_space_refine*
824 was performed with only rigid-body refinement enabled; each large and small subdomain of each
825 protomer was treated as a single rigid body (twelve total). Nucleotides and water molecules were
826 then added where appropriate. Subsequent cycles of manual model building were performed in
827 *Coot* and *ISOLDE* followed by 1–7 macrocycles of *phenix.real_space_refine* with global
828 minimization and local grid search enabled. Ramachandran and secondary structure restraints
829 were used throughout.

830 The previously described reference models were then used as starting models in building the
831 sx20S and bin20S supercomplexes. In sx20S and bin20S reconstructions with well-defined N-
832 domains (i.e., a recognizable two-lobed density), one or more instances of the re-processed
833 model derived from the crystal structure (PDB ID 1QCS[88]) as re-processed by *PDB_REDO*[89]
834 were rigid body fit into density before refinement. Next, the appropriate α-SNAP—SNARE
835 subcomplex was docked into the density, completing the spire structure. Spires in the global 20S
836 reconstructions were generally heterogeneous; although secondary structure could often be
837 distinguished, side chain density could not, leading to poor map-model correlations in these
838 regions. A round of *phenix.real_space_refine* was performed with only rigid-body refinement
839 enabled; each large and small subdomain of each protomer, each N domain, and each α-SNAP—
840 SNARE subcomplex was treated as a rigid body (for a 20S particle with four engaged N-
841 domains, this would be 17 total rigid body groups). Nucleotides, Mg^{2+}, P_i, and water molecules
842 were then added where appropriate. Subsequent cycles of manual model building were
843 performed in *Coot* and *ISOLDE* followed by 1–7 macrocycles of *phenix.real_space_refine* with
844 global minimization and local grid search enabled. Ramachandran and secondary structure
845 restraints were used throughout.

846 All model figures were prepared with *UCSF ChimeraX*, in many cases with custom CXC scripts
847 generated by the Python scripts described below.

848 **Automated NSF model analysis and coordinate PCA**

849 Several custom Python scripts (*preprocess_models.py, analyze_models.py*) using the *Bio.PDB*
850 module[90] of the Biopython project[91] as well as *pandas*[71], *numpy*[72], *scipy*[73], *scikit-learn*[92], and
851 *matplotlib*[74] were used to standardize all 25 NSF, sx20S, or bin20S models for further analysis,
852 such as to perform principle components analysis (PCA) and HDBSCAN clustering, to measure

853 NSF D1 large-small subdomain angles, to perform planarity fits for NSF domains and
854 subdomains, to measure distances between key catalytic residues and nucleotides, and to map
855 various values to structures for visualization in *UCSF ChimeraX*.

856 For PCA, 132 NSF D1 domains from 22 models over all datasets were split into large and small
857 subdomains, which were then aligned to one another (large, residues 224–373; small, residues
858 400–486) using *Bio.PDB.Superimposer*. Splitting removes the largest source of variance in the
859 data, the rigid body motions of the two subdomains relative to each other, which is considered
860 trivial for the purposes of this analysis. Next, a Cα coordinate matrix **C** with dimensions $n_{models} \times$
861 $n_{residues} \times 3$ was constructed for residues shared by all models and flattened into two dimensions,
862 creating $\mathbf{C_{flat}}$ with n_{models} rows and $n_{residues} \times 3$ columns. $\mathbf{C_{flat}}$ was then rescaled using
863 *sklearn.preprocessing.StandardScaler* and PCA was performed on $\mathbf{C_{flat}}$ using
864 *sklearn.decomposition.PCA*. 13 components were found to contribute 99% of the variance, so a
865 transformed matrix $\mathbf{C_{trans}}$ with dimensions $n_{models} \times 13$, with eigenvectors sorted along the second
866 axis by eigenvalue, was calculated. The cluster analysis of models was then performed using
867 *sklearn.cluster.HDBSCAN* with a minimum cluster size of three, producing 11 clusters
868 accounting for 119/132 total models. This analysis serves as the basis for Fig. 8A.

869 For NSF D1 and D2 plane fits, centers of mass for all subdomains were calculated, and the
870 planes for different combinations of these points were fit using a least squares approach
871 (Supplementary Fig. 8). For NSF D1 large-small subdomain angle calculations, the primary axes
872 of two α-helices in the large (residues 350–358) and small subdomains (residues 442–452) were
873 calculated by singular value decomposition using *np.linalg.svd*, with implementation inspired by
874 *helix_analysis.py* from the MDAnalysis package[93]. Vectors corresponding to these helical axes *u*

875 and v were normalized and centered at the coordinate origin, and the angle between them was

876 calculated as $\theta = 2 \times \tan^{-1}\left(\sqrt{\sum_i \vec{u}_i^2}\sqrt{\sum_i \vec{v}_i^2}\right)$.

877 Distances between key active site atoms over all models (Fig. 9) were calculated using

878 *np.linalg.norm*, where the norm of the difference vector of the coordinates of each atom is the

879 distance between them in Å. Significant changes in protomer E active site residues relative to the

880 other five protomers were assessed by pairwise application of the Welch's t-test assuming non-

881 equal variances as implemented in *scipy.stats.ttest_ind*. Distance distributions were considered

882 statistically different if $p < 0.05$.

883 All these values, as well as manually curated, qualitative data labels, were plotted in various

884 ways using *matplotlib* or incorporated into automatically generated UCSF *ChimeraX* CXC

885 scripts.

886 # Data availability

887 The atomic coordinates have been deposited in the Protein Data Bank (PDB) under accession
888 codes 9OJ2 [http://doi.org/10.2210/pdb9oj2/pdb] (sx20S complex (NSF-alphaSNAP-syntaxin-
889 1a), non-hydrolyzing, class 1); 9OJJ [http://doi.org/10.2210/pdb9ojj/pdb] (sx20S complex (NSF-
890 alphaSNAP-syntaxin-1a), alphaSNAP-syntaxin-1a subcomplex local refinement, non-
891 hydrolyzing, class 1); 9OJR [http://doi.org/10.2210/pdb9ojr/pdb] (21bin20S complex (NSF-
892 alphaSNAP-2:1 syntaxin-1a:SNAP-25), non-hydrolyzing, class 3); 9OJU
893 [http://doi.org/10.2210/pdb9oju/pdb] (21bin20S complex (NSF-alphaSNAP-2:1 syntaxin-
894 1a:SNAP-25), non-hydrolyzing, class 4); 9OJZ [http://doi.org/10.2210/pdb9ojz/pdb] (21bin20S
895 complex (NSF-alphaSNAP-2:1 syntaxin-1a:SNAP-25), non-hydrolyzing, class 5); 9OK3
896 [http://doi.org/10.2210/pdb9ok3/pdb] (21bin20S complex (NSF-alphaSNAP-2:1 syntaxin-
897 1a:SNAP-25), 3:2:1 alphaSNAP-syntaxin-1a-SNAP-25 subcomplex local refinement, non-
898 hydrolyzing, class 13); 9OK5 [http://doi.org/10.2210/pdb9ok5/pdb] (22bin20S complex (NSF-
899 alphaSNAP-2:2 syntaxin-1a:SNAP-25), hydrolyzing, class 16); 9OKC
900 [http://doi.org/10.2210/pdb9okc/pdb] (22bin20S complex (NSF-alphaSNAP-2:2 syntaxin-
901 1a:SNAP-25), hydrolyzing, class 17); 9OLJ [http://doi.org/10.2210/pdb9olj/pdb] (22bin20S
902 complex (NSF-alphaSNAP-2:2 syntaxin-1a:SNAP-25), hydrolyzing, class 18); 9OLO
903 [http://doi.org/10.2210/pdb9olo/pdb] (22bin20S complex (NSF-alphaSNAP-2:2 syntaxin-
904 1a:SNAP-25), hydrolyzing, class 19); 9OM6 [http://doi.org/10.2210/pdb9om6/pdb] (22bin20S
905 complex (NSF-alphaSNAP-2:2 syntaxin-1a:SNAP-25), 4:2:2 alphaSNAP-syntaxin-1a-SNAP-25
906 subcomplex local refinement, hydrolyzing, class 23); 9OMQ
907 [http://doi.org/10.2210/pdb9omq/pdb] (NSF, substrate free, hydrolyzing, class 24); 9PAF
908 [http://doi.org/10.2210/pdb9paf/pdb] (21bin20S complex (NSF-alphaSNAP-2:1 syntaxin-

1a:SNAP-25), non-hydrolyzing, class 6); 9PAG [http://doi.org/10.2210/pdb9pag/pdb] (21bin20S complex (NSF-alphaSNAP-2:1 syntaxin-1a:SNAP-25), non-hydrolyzing, class 7); 9PB9 [http://doi.org/10.2210/pdb9pb9/pdb] (21bin20S complex (NSF-alphaSNAP-2:1 syntaxin-1a:SNAP-25), non-hydrolyzing, class 8); 9PBA [http://doi.org/10.2210/pdb9pba/pdb] (21bin20S complex (NSF-alphaSNAP-2:1 syntaxin-1a:SNAP-25), non-hydrolyzing, class 9); 9PBF [http://doi.org/10.2210/pdb9pbf/pdb] (21bin20S complex (NSF-alphaSNAP-2:1 syntaxin-1a:SNAP-25), non-hydrolyzing, class 10); 9PBV [http://doi.org/10.2210/pdb9pbv/pdb] (21bin20S complex (NSF-alphaSNAP-2:1 syntaxin-1a:SNAP-25), non-hydrolyzing, class 11); 9PC3 [http://doi.org/10.2210/pdb9pc3/pdb] (21bin20S complex (NSF-alphaSNAP-2:1 syntaxin-1a:SNAP-25), non-hydrolyzing, class 12); 9PCX [http://doi.org/10.2210/pdb9pcx/pdb] (22bin20S complex (NSF-alphaSNAP-2:2 syntaxin-1a:SNAP-25), hydrolyzing, class 14); 9PCZ [http://doi.org/10.2210/pdb9pcz/pdb] (22bin20S complex (NSF-alphaSNAP-2:2 syntaxin-1a:SNAP-25), hydrolyzing, class 15); 9PD1 [http://doi.org/10.2210/pdb9pd1/pdb] (22bin20S complex (NSF-alphaSNAP-2:2 syntaxin-1a:SNAP-25), hydrolyzing, class 20); 9PD8 [http://doi.org/10.2210/pdb9pd8/pdb] (22bin20S complex (NSF-alphaSNAP-2:2 syntaxin-1a:SNAP-25), hydrolyzing, class 21); 9PDB [http://doi.org/10.2210/pdb9pdb/pdb] (22bin20S complex (NSF-alphaSNAP-2:2 syntaxin-1a:SNAP-25), hydrolyzing, class 22); 9PDD [http://doi.org/10.2210/pdb9pdd/pdb] (22bin20S complex (NSF-alphaSNAP-2:2 syntaxin-1a:SNAP-25), hydrolyzing, class 29); 9PF2 [http://doi.org/10.2210/pdb9pf2/pdb] (NSF, substrate free, hydrolyzing, class 25); 9PFC [http://doi.org/10.2210/pdb9pfc/pdb] (NSF, substrate free, hydrolyzing, class 26); 9PFF [http://doi.org/10.2210/pdb9pff/pdb] (min22bin20S complex (NSF-alphaSNAP-2:2 syntaxin-1a H3:SNAP-25 SN1), non-hydrolyzing, class 27); and 9PFG [http://doi.org/10.2210/pdb9pfg/pdb] (min22bin20S complex (NSF-alphaSNAP-2:2 syntaxin-1a

932 H3:SNAP-25 SN1), 4:2:2 alphaSNAP-syntaxin-1a H3-SNAP-25 SN1 subcomplex local
933 refinement, non-hydrolyzing, class 28). Previously published models used in this work include
934 6MDM [http://doi.org/10.2210/pdb6mdm/pdb] (The 20S supercomplex engaging the SNAP-25
935 N-terminus (class 1)); 1N7S [http://doi.org/10.2210/pdb1n7s/pdb] (High Resolution Structure of
936 a Truncated Neuronal SNARE Complex); 1QCS [http://doi.org/10.2210/pdb1qcs/pdb] (N-
937 TERMINAL DOMAIN OF N-ETHYLMALEIMIDE SENSITIVE FACTOR (NSF)); 1JTH
938 [http://doi.org/10.2210/pdb1jth/pdb] (Crystal structure and biophysical properties of a complex
939 between the N-terminal region of SNAP25 and the SNARE region of syntaxin 1a); and 1HVV
940 [http://doi.org/10.2210/pdb1hvv/pdb] (SELF-ASSOCIATION OF THE H3 REGION OF
941 SYNTAXIN 1A).

942 Code Availability

943 We used *AlphaFold2*[94], *ChimeraX 1.6–1.8*[84], *Coot 0.9*[83], *CryoSPARC*[57,80], *CTFFIND4*[77],
944 *ImageJ*[67], *ISOLDE*[85], *MolProbity*[95], *MotionCorr2*[76], *PHENIX 1.2.X*[86,87,96], *Prism* (GraphPad
945 Software), *RELION 3*[78], *Segger*[81], and *SerialEM 4*[75]. Custom scripts were written in *Python 3.1*
946 with packages including *numpy*[72], *scipy*[73], *scikit-learn*[92], *biopython*[90,91], *pandas*[71], and
947 *matplotlib*[74] and are available at https://github.com/brungerlab/kiw_scripts.

948 References

949 1. Rizo, J., and Südhof, T.C. (2012). The membrane fusion enigma: SNAREs, Sec1/Munc18
950 proteins, and their accomplices--guilty as charged? Annu. Rev. Cell Dev. Biol. *28*, 279–308.
951 https://doi.org/10.1146/annurev-cellbio-101011-155818.

952 2. Brunger, A.T., Choi, U.B., Lai, Y., Leitz, J., and Zhou, Q. (2018). Molecular Mechanisms of
953 Fast Neurotransmitter Release. Annu. Rev. Biophys. *47*, 469–497.
954 https://doi.org/10.1146/annurev-biophys-070816-034117.

955 3. Leitz, J., Wang, C., Esquivies, L., Pfuetzner, R.A., Peters, J.J., Couoh-Cardel, S., Wang,
956 A.L., and Brunger, A.T. (2024). Beyond the MUN domain, Munc13 controls priming and
957 depriming of synaptic vesicles. Cell Rep. *43*. https://doi.org/10.1016/j.celrep.2024.114026.

958 4. Brunger, A.T., Choi, U.B., Lai, Y., Leitz, J., White, K.I., and Zhou, Q. (2019). The pre-
959 synaptic fusion machinery. Curr. Opin. Struct. Biol. *54*, 179–188.
960 https://doi.org/10.1016/j.sbi.2019.03.007.

961 5. Rizo, J. (2022). Molecular Mechanisms Underlying Neurotransmitter Release. Annu. Rev.
962 Biophys. *51*, 377–408. https://doi.org/10.1146/annurev-biophys-111821-104732.

963 6. White, K.I., Zhao, M., Choi, U.B., Pfuetzner, R.A., and Brunger, A.T. (2018). Structural
964 principles of SNARE complex recognition by the AAA+ protein NSF. eLife *7*, e38888.
965 https://doi.org/10.7554/eLife.38888.

966 7. Zhao, M., Wu, S., Zhou, Q., Vivona, S., Cipriano, D.J., Cheng, Y., and Brunger, A.T.
967 (2015). Mechanistic insights into the recycling machine of the SNARE complex. Nature *518*,
968 61–67. https://doi.org/10.1038/nature14148.

969 8. Rickman, C., Medine, C.N., Dun, A.R., Moulton, D.J., Mandula, O., Halemani, N.D.,
970 Rizzoli, S.O., Chamberlain, L.H., and Duncan, R.R. (2010). t-SNARE Protein
971 Conformations Patterned by the Lipid Microenvironment. J. Biol. Chem. *285*, 13535–13541.
972 https://doi.org/10.1074/jbc.M109.091058.

973 9. Murray, D.H., and Tamm, L.K. (2009). Clustering of Syntaxin-1A in Model Membranes is
974 Modulated by Phosphatidylinositol-4,5-bisphosphate and Cholesterol. Biochemistry *48*,
975 4617–4625. https://doi.org/10.1021/bi9003217.

976 10. Aoyagi, K., Sugaya, T., Umeda, M., Yamamoto, S., Terakawa, S., and Takahashi, M. (2005).
977 The activation of exocytotic sites by the formation of phosphatidylinositol 4,5-bisphosphate
978 microdomains at syntaxin clusters. J. Biol. Chem. *280*, 17346–17352.
979 https://doi.org/10.1074/jbc.M413307200.

980 11. Lang, T., Bruns, D., Wenzel, D., Riedel, D., Holroyd, P., Thiele, C., and Jahn, R. (2001).
981 SNAREs are concentrated in cholesterol-dependent clusters that define docking and fusion
982 sites for exocytosis. EMBO J. *20*, 2202–2213. https://doi.org/10.1093/emboj/20.9.2202.

983 12. Emperador-Melero, J., and Kaeser, P.S. (2020). Assembly of the presynaptic active zone.
984 Curr. Opin. Neurobiol. *63*, 95–103. https://doi.org/10.1016/j.conb.2020.03.008.

985 13. Sieber, J.J., Willig, K.I., Kutzner, C., Gerding-Reimers, C., Harke, B., Donnert, G.,
986 Rammner, B., Eggeling, C., Hell, S.W., Grubmüller, H., et al. (2007). Anatomy and
987 Dynamics of a Supramolecular Membrane Protein Cluster. Science *317*, 1072–1076.
988 https://doi.org/10.1126/science.1141727.

989 14. Weimbs, T., Low, S.H., Chapin, S.J., Mostov, K.E., Bucher, P., and Hofmann, K. (1997). A
990 conserved domain is present in different families of vesicular fusion proteins:
991 A new superfamily. Proc. Natl. Acad. Sci. U. S. A. *94*, 3046–3051.

992 15. Bennett, M.K., Calakos, N., and Scheller, R.H. (1992). Syntaxin: A Synaptic Protein
993 Implicated in Docking of Synaptic Vesicles at Presynaptic Active Zones. Science *257*, 255–
994 259. https://doi.org/10.1126/science.1321498.

995 16. Sutton, R.B., Fasshauer, D., Jahn, R., and Brunger, A.T. (1998). Crystal structure of a
996 SNARE complex involved in synaptic exocytosis at 2.4 Å resolution. Nature *395*, 347–353.
997 https://doi.org/10.1038/26412.

998 17. Fernandez, I., Ubach, J., Dulubova, I., Zhang, X., Südhof, T.C., and Rizo, J. (1998). Three-
999 Dimensional Structure of an Evolutionarily Conserved N-Terminal Domain of Syntaxin 1A.
1000 Cell *94*, 841–849. https://doi.org/10.1016/s0092-8674(00)81742-0.

1001 18. Bar-On, D., Wolter, S., Van De Linde, S., Heilemann, M., Nudelman, G., Nachliel, E.,
1002 Gutman, M., Sauer, M., and Ashery, U. (2012). Super-resolution Imaging Reveals the
1003 Internal Architecture of Nano-sized Syntaxin Clusters. J. Biol. Chem. *287*, 27158–27167.
1004 https://doi.org/10.1074/jbc.M112.353250.

1005 19. Knowles, M.K., Barg, S., Wan, L., Midorikawa, M., Chen, X., and Almers, W. (2010).
1006 Single secretory granules of live cells recruit syntaxin-1 and synaptosomal associated protein
1007 25 (SNAP-25) in large copy numbers. Proc. Natl. Acad. Sci. *107*, 20810–20815.
1008 https://doi.org/10.1073/pnas.1014840107.

1009 20. Wan, L., Chen, X., and Almers, W. (2021). Munc18-dependent and -independent clustering
1010 of syntaxin in the plasma membrane of cultured endocrine cells. Proc. Natl. Acad. Sci. *118*,
1011 e2025748118. https://doi.org/10.1073/pnas.2025748118.

1012 21. Ullrich, A., Böhme, M.A., Schöneberg, J., Depner, H., Sigrist, S.J., and Noé, F. (2015).
1013 Dynamical Organization of Syntaxin-1A at the Presynaptic Active Zone. PLOS Comput.
1014 Biol. *11*, e1004407. https://doi.org/10.1371/journal.pcbi.1004407.

1015 22. Barg, S., Knowles, M.K., Chen, X., Midorikawa, M., and Almers, W. (2010). Syntaxin
1016 clusters assemble reversibly at sites of secretory granules in live cells. Proc. Natl. Acad. Sci.
1017 *107*, 20804–20809. https://doi.org/10.1073/pnas.1014823107.

1018 23. Sakamoto, H., Ariyoshi, T., Kimpara, N., Sugao, K., Taiko, I., Takikawa, K., Asanuma, D.,
1019 Namiki, S., and Hirose, K. (2018). Synaptic weight set by Munc13-1 supramolecular
1020 assemblies. Nat. Neurosci. *21*, 41–49. https://doi.org/10.1038/s41593-017-0041-9.

1021 24. Pertsinidis, A., Mukherjee, K., Sharma, M., Pang, Z.P., Park, S.R., Zhang, Y., Brunger, A.T.,
1022 Südhof, T.C., and Chu, S. (2013). Ultrahigh-resolution imaging reveals formation of
1023 neuronal SNARE/Munc18 complexes in situ. Proc. Natl. Acad. Sci. *110*, E2812–E2820.
1024 https://doi.org/10.1073/pnas.1310654110.

1025 25. Yin, P., Gandasi, N.R., Arora, S., Omar-Hmeadi, M., Saras, J., and Barg, S. (2018). Syntaxin
1026 clusters at secretory granules in a munc18-bound conformation. Mol. Biol. Cell *29*, 2700–
1027 2708. https://doi.org/10.1091/mbc.E17-09-0541.

1028 26. Lang, T. (2007). SNARE proteins and ‘membrane rafts.’ J. Physiol. *585*, 693–698.
1029 https://doi.org/10.1113/jphysiol.2007.134346.

1030 27. Bademosi, A.T., Lauwers, E., Padmanabhan, P., Odierna, L., Chai, Y.J., Papadopulos, A.,
1031 Goodhill, G.J., Verstreken, P., van Swinderen, B., and Meunier, F.A. (2016). In vivo single-
1032 molecule imaging of syntaxin1A reveals polyphosphoinositide- and activity-dependent
1033 trapping in presynaptic nanoclusters. Nat. Commun. *7*, 13660.
1034 https://doi.org/10.1038/ncomms13660.

1035 28. Sieber, J.J., Willig, K.I., Heintzmann, R., Hell, S.W., and Lang, T. (2006). The SNARE
1036 Motif Is Essential for the Formation of Syntaxin Clusters in the Plasma Membrane. Biophys.
1037 J. *90*, 2843–2851. https://doi.org/10.1529/biophysj.105.079574.

1038 29. Hanson, P.I., Otto, H., Barton, N., and Jahn, R. (1995). The N-Ethylmaleimide-sensitive
1039 Fusion Protein and α-SNAP Induce a Conformational Change in Syntaxin (*). J. Biol. Chem.
1040 *270*, 16955–16961. https://doi.org/10.1074/jbc.270.28.16955.

1041 30. Stepien, K.P., Prinslow, E.A., and Rizo, J. (2019). Munc18-1 is crucial to overcome the
1042 inhibition of synaptic vesicle fusion by αSNAP. Nat. Commun. *10*, 4326.
1043 https://doi.org/10.1038/s41467-019-12188-4.

1044 31. Ma, C., Su, L., Seven, A.B., Xu, Y., and Rizo, J. (2013). Reconstitution of the vital functions
1045 of Munc18 and Munc13 in neurotransmitter release. Science *339*, 421–425.
1046 https://doi.org/10.1126/science.1230473.

1047 32. Choi, U.B., Zhao, M., White, K.I., Pfuetzner, R.A., Esquivies, L., Zhou, Q., and Brunger,
1048 A.T. (2018). NSF-mediated disassembly of on- and off-pathway SNARE complexes and
1049 inhibition by complexin. eLife *7*, e36497. https://doi.org/10.7554/eLife.36497.

1050 33. Fasshauer, D., Bruns, D., Shen, B., Jahn, R., and Brunger, A.T. (1997). A Structural Change
1051 Occurs upon Binding of Syntaxin to SNAP-25. J. Biol. Chem. *272*, 4582–4590.
1052 https://doi.org/10.1074/jbc.272.7.4582.

1053 34. Misura, K.M.S., Gonzalez, L.C., May, A.P., Scheller, R.H., and Weis, W.I. (2001). Crystal
1054 Structure and Biophysical Properties of a Complex between the N-terminal SNARE Region
1055 of SNAP25 and Syntaxin 1a *. J. Biol. Chem. *276*, 41301–41309.
1056 https://doi.org/10.1074/jbc.M106853200.

1057 35. Weninger, K., Bowen, M.E., Choi, U.B., Chu, S., and Brunger, A.T. (2008). Accessory
1058 Proteins Stabilize the Acceptor Complex for Synaptobrevin, the 1:1 Syntaxin/SNAP-25
1059 Complex. Structure *16*, 308–320. https://doi.org/10.1016/j.str.2007.12.010.

1060 36. Hesselbarth, J., and Schmidt, C. (2023). Mass spectrometry uncovers intermediates and off-
1061 pathway complexes for SNARE complex assembly. Commun. Biol. *6*, 1–15.
1062 https://doi.org/10.1038/s42003-023-04548-0.

1063 37. Hayashi, T., McMahon, H., Yamasaki, S., Binz, T., Hata, Y., Südhof, T.C., and Niemann, H.
1064 (1994). Synaptic vesicle membrane fusion complex: action of clostridial neurotoxins on
1065 assembly. EMBO J. *13*, 5051–5061. https://doi.org/10.1002/j.1460-2075.1994.tb06834.x.

1066 38. Gao, Y., Khan, Y.A., Mo, W., White, K.I., Perkins, M., Pfuetzner, R.A., Trapani, J.G.,
1067 Brunger, A.T., and Nicolson, T. (2023). Sensory deficit screen identifies nsf mutation that
1068 differentially affects SNARE recycling and quality control. Cell Rep. *42*.
1069 https://doi.org/10.1016/j.celrep.2023.112345.

1070 39. Hayashi, T., Yamasaki, S., Nauenburg, S., Binz, T., and Niemann, H. (1995). Disassembly of
1071 the reconstituted synaptic vesicle membrane fusion complex in vitro. EMBO J. *14*, 2317–
1072 2325. https://doi.org/10.1002/j.1460-2075.1995.tb07226.x.

1073 40. Vivona, S., Cipriano, D.J., O'Leary, S., Li, Y.H., Fenn, T.D., and Brunger, A.T. (2013).
1074 Disassembly of All SNARE Complexes by N-Ethylmaleimide-sensitive Factor (NSF) Is
1075 Initiated by a Conserved 1:1 Interaction between α-Soluble NSF Attachment Protein (SNAP)
1076 and SNARE Complex. J. Biol. Chem. *288*, 24984–24991.
1077 https://doi.org/10.1074/jbc.M113.489807.

1078 42. Nagiec, E.E., Bernstein, A., and Whiteheart, S.W. (1995). Each Domain of the N-
1079 Ethylmaleimide-sensitive Fusion Protein Contributes to Its Transport Activity (*). J. Biol.
1080 Chem. *270*, 29182–29188. https://doi.org/10.1074/jbc.270.49.29182.

1081 43. Matveeva, E.A., He, P., and Whiteheart, S.W. (1997). N-Ethylmaleimide-sensitive Fusion
1082 Protein Contains High and Low Affinity ATP-binding Sites That Are Functionally Distinct
1083 *. J. Biol. Chem. *272*, 26413–26418. https://doi.org/10.1074/jbc.272.42.26413.

1084 44. Donovan, K.W., and Bretscher, A. (2015). Tracking individual secretory vesicles during
1085 exocytosis reveals an ordered and regulated process. J. Cell Biol. *210*, 181–189.
1086 https://doi.org/10.1083/jcb.201501118.

1087 45. Khan, Y.A., White, K.I., Pfuetzner, R.A., Singal, B., Esquivies, L., Mckenzie, G., Liu, F.,
1088 DeLong, K., Choi, U.B., Montabana, E., et al. (2025). SNARE disassembly requires
1089 Sec18/NSF side loading. Nat. Struct. Mol. Biol., 1–13. https://doi.org/10.1038/s41594-025-
1090 01590-w.

1091 46. Stepien, K.P., Xu, J., Zhang, X., Bai, X.-C., and Rizo, J. (2022). SNARE assembly
1092 enlightened by cryo-EM structures of a synaptobrevin–Munc18-1–syntaxin-1 complex. Sci.
1093 Adv. *8*, eabo5272. https://doi.org/10.1126/sciadv.abo5272.

1094 47. Dawidowski, D., and Cafiso, D.S. (2013). Allosteric Control of Syntaxin 1a by Munc18-1:
1095 Characterization of the Open and Closed Conformations of Syntaxin. Biophys. J. *104*, 1585.
1096 https://doi.org/10.1016/j.bpj.2013.02.004.

1097 48. Pei, Q., Chen, Q., Tian, Z., Zhu, L., Chen, Y., Gong, J., Wang, S., Xiang, Y., Khamo, J., Fan,
1098 J., et al. (2024). Munc18 modulates syntaxin phase separation for exocytosis.

1099 49. Meijer, M., Burkhardt, P., de Wit, H., Toonen, R.F., Fasshauer, D., and Verhage, M. (2012).
1100 Munc18-1 mutations that strongly impair SNARE-complex binding support normal synaptic
1101 transmission. EMBO J. *31*, 2156–2168. https://doi.org/10.1038/emboj.2012.72.

1102 50. Xiao, W., Poirier, M.A., Bennett, M.K., and Shin, Y.-K. (2001). The neuronal t-SNARE
1103 complex is a parallel four-helix bundle. Nat. Struct. Biol. *8*, 308–311.
1104 https://doi.org/10.1038/86174.

1105 51. Margittai, M., Fasshauer, D., Pabst, S., Jahn, R., and Langen, R. (2001). Homo- and
1106 Heterooligomeric SNARE Complexes Studied by Site-directed Spin Labeling *. J. Biol.
1107 Chem. *276*, 13169–13177. https://doi.org/10.1074/jbc.M010653200.

1108 52. Lai, Y., Choi, U.B., Leitz, J., Rhee, H.J., Lee, C., Altas, B., Zhao, M., Pfuetzner, R.A.,
1109 Wang, A.L., Brose, N., et al. (2017). Molecular Mechanisms of Synaptic Vesicle Priming by
1110 Munc13 and Munc18. Neuron *95*, 591-607.e10.
1111 https://doi.org/10.1016/j.neuron.2017.07.004.

1112 53. Sanyal, S., and Krishnan, K.S. (2001). Lethal comatose mutation in Drosophila reveals
1113 possible role for NSF in neurogenesis. NeuroReport *12*, 1363.

1114 54. Ernst, J.A., and Brunger, A.T. (2003). High Resolution Structure, Stability, and
1115 Synaptotagmin Binding of a Truncated Neuronal SNARE Complex *. J. Biol. Chem. *278*,
1116 8630–8636. https://doi.org/10.1074/jbc.M211889200.

1117 55. Pribicevic, S., Graham, A.C., Cafiso, D.S., Pérez-Lara, Á., and Jahn, R. (2024). Intermediate
1118 steps in the formation of neuronal SNARE complexes. J. Biol. Chem. *300*, 107591.
1119 https://doi.org/10.1016/j.jbc.2024.107591.

1120 56. de la Peña, A.H., Goodall, E.A., Gates, S.N., Lander, G.C., and Martin, A. (2018). Substrate-
1121 engaged 26S proteasome structures reveal mechanisms for ATP-hydrolysis–driven
1122 translocation. Science *362*, eaav0725. https://doi.org/10.1126/science.aav0725.

1123 57. Punjani, A., and Fleet, D.J. (2021). 3D variability analysis: Resolving continuous flexibility
1124 and discrete heterogeneity from single particle cryo-EM. J. Struct. Biol. *213*, 107702.
1125 https://doi.org/10.1016/j.jsb.2021.107702.

1126 58. Smith, G.R., Contreras-Moreira, B., Zhang, X., and Bates, P.A. (2004). A link between
1127 sequence conservation and domain motion within the AAA+ family. J. Struct. Biol. *146*,
1128 189–204. https://doi.org/10.1016/j.jsb.2003.11.022.

1129 59. Zhou, H., Di Palma, S., Preisinger, C., Peng, M., Polat, A.N., Heck, A.J.R., and Mohammed,
1130 S. (2013). Toward a Comprehensive Characterization of a Human Cancer Cell
1131 Phosphoproteome. J. Proteome Res. *12*, 260–271. https://doi.org/10.1021/pr300630k.

1132 60. Matveeva, E.A., Whiteheart, S.W., Vanaman, T.C., and Slevin, J.T. (2001). Phosphorylation
1133 of the N-Ethylmaleimide-sensitive Factor Is Associated with Depolarization-dependent
1134 Neurotransmitter Release from Synaptosomes. J. Biol. Chem. *276*, 12174–12181.
1135 https://doi.org/10.1074/jbc.m007394200.

1136 61. Huang, X., Sun, S., Wang, X., Fan, F., Zhou, Q., Lu, S., Cao, Y., Wang, Q.-W., Dong, M.-
1137 Q., Yao, J., et al. (2019). Mechanistic insights into the SNARE complex disassembly. Sci.
1138 Adv. *5*, eaau8164. https://doi.org/10.1126/sciadv.aau8164.

1139 62. Mertins, J., Finke, J., Sies, R., Rink, K.M., Hasenauer, J., and Lang, T. (2021). The
1140 mesoscale organization of syntaxin 1A and SNAP25 is determined by SNARE–SNARE
1141 interactions. eLife *10*, e69236. https://doi.org/10.7554/eLife.69236.

1142 63. Kraichely, K.N., Sandall, C.R., Liang, B., Kiessling, V., and Tamm, L.K. (2025).
1143 Functionally distinct SNARE motifs of SNAP25 cooperate in SNARE assembly and
1144 membrane fusion. Biophys. J. *124*, 637–650. https://doi.org/10.1016/j.bpj.2024.12.034.

1145 64. Zhou, Q., Zhou, P., Wang, A.L., Wu, D., Zhao, M., Südhof, T.C., and Brunger, A.T. (2017).
1146 The primed SNARE–complexin–synaptotagmin complex for neuronal exocytosis. Nature
1147 *548*, 420–425. https://doi.org/10.1038/nature23484.

1148 65. Zhou, Q., Lai, Y., Bacaj, T., Zhao, M., Lyubimov, A.Y., Uervirojnangkoorn, M., Zeldin,
1149 O.B., Brewster, A.S., Sauter, N.K., Cohen, A.E., et al. (2015). Architecture of the
1150 synaptotagmin–SNARE machinery for neuronal exocytosis. Nature *525*, 62–67.
1151 https://doi.org/10.1038/nature14975.

1152 66. Khan, Y.A., White, K.I., and Brunger, A.T. (2022). The AAA+ superfamily: a review of the
1153 structural and mechanistic principles of these molecular machines. Crit. Rev. Biochem. Mol.
1154 Biol. *57*, 156–187. https://doi.org/10.1080/10409238.2021.1979460.

1155 67. Schneider, C.A., Rasband, W.S., and Eliceiri, K.W. (2012). NIH Image to ImageJ: 25 years
1156 of image analysis. Nat. Methods *9*, 671–675. https://doi.org/10.1038/nmeth.2089.

1157 68. Yofe, I., Weill, U., Meurer, M., Chuartzman, S., Zalckvar, E., Goldman, O., Ben-Dor, S.,
1158 Schütze, C., Wiedemann, N., Knop, M., et al. (2016). One library to make them all:
1159 streamlining the creation of yeast libraries via a SWAp-Tag strategy. Nat. Methods *13*, 371–
1160 378. https://doi.org/10.1038/nmeth.3795.

1161 69. Cipriano, D.J., Jung, J., Vivona, S., Fenn, T.D., Brunger, A.T., and Bryant, Z. (2013).
1162 Processive ATP-driven Substrate Disassembly by the N-Ethylmaleimide-sensitive Factor
1163 (NSF) Molecular Machine♦. J. Biol. Chem. *288*, 23436–23445.
1164 https://doi.org/10.1074/jbc.M113.476705.

1165 70. Studier, F.W. (2005). Protein production by auto-induction in high-density shaking cultures.
1166 Protein Expr. Purif. *41*, 207–234. https://doi.org/10.1016/j.pep.2005.01.016.

1167 71. McKinney, W. (2010). Data Structures for Statistical Computing in Python. In Proceedings
1168 of the 9th Python in Science Confference, pp. 56–61. https://doi.org/10.25080/Majora-
1169 92bf1922-00a.

1170 72. Harris, C.R., Millman, K.J., van der Walt, S.J., Gommers, R., Virtanen, P., Cournapeau, D.,
1171 Wieser, E., Taylor, J., Berg, S., Smith, N.J., et al. (2020). Array programming with NumPy.
1172 Nature *585*, 357–362. https://doi.org/10.1038/s41586-020-2649-2.

1173 73. Virtanen, P., Gommers, R., Oliphant, T.E., Haberland, M., Reddy, T., Cournapeau, D.,
1174 Burovski, E., Peterson, P., Weckesser, W., Bright, J., et al. (2020). SciPy 1.0: fundamental
1175 algorithms for scientific computing in Python. Nat. Methods *17*, 261–272.
1176 https://doi.org/10.1038/s41592-019-0686-2.

1177 74. Hunter, J.D. (2007). Matplotlib: A 2D Graphics Environment. Comput. Sci. Eng. *9*, 90–95.
1178 https://doi.org/10.1109/MCSE.2007.55.

1179 75. Mastronarde, D.N. (2005). Automated electron microscope tomography using robust
1180 prediction of specimen movements. J. Struct. Biol. *152*, 36–51.
1181 https://doi.org/10.1016/j.jsb.2005.07.007.

1182 76. Zheng, S.Q., Palovcak, E., Armache, J.-P., Verba, K.A., Cheng, Y., and Agard, D.A. (2017).
1183 MotionCor2 - anisotropic correction of beam-induced motion for improved cryo-electron
1184 microscopy. Nat. Methods *14*, 331–332. https://doi.org/10.1038/nmeth.4193.

1185 77. Rohou, A., and Grigorieff, N. (2015). CTFFIND4: Fast and accurate defocus estimation from
1186 electron micrographs. J. Struct. Biol. *192*, 216–221.
1187 https://doi.org/10.1016/j.jsb.2015.08.008.

1188 78. Scheres, S.H.W. (2012). RELION: Implementation of a Bayesian approach to cryo-EM
1189 structure determination. J. Struct. Biol. *180*, 519–530.
1190 https://doi.org/10.1016/j.jsb.2012.09.006.

1191 79. Zivanov, J., Nakane, T., Forsberg, B.O., Kimanius, D., Hagen, W.J., Lindahl, E., and
1192 Scheres, S.H. (2018). New tools for automated high-resolution cryo-EM structure
1193 determination in RELION-3. eLife *7*, e42166. https://doi.org/10.7554/eLife.42166.

1194 80. Punjani, A., Rubinstein, J.L., Fleet, D.J., and Brubaker, M.A. (2017). cryoSPARC:
1195 algorithms for rapid unsupervised cryo-EM structure determination. Nat. Methods *14*, 290–
1196 296. https://doi.org/10.1038/nmeth.4169.

1197 81. Pintilie, G.D., Zhang, J., Goddard, T.D., Chiu, W., and Gossard, D.C. (2010). Quantitative
1198 analysis of cryo-EM density map segmentation by watershed and scale-space filtering, and
1199 fitting of structures by alignment to regions. J. Struct. Biol. *170*, 427–438.
1200 https://doi.org/10.1016/j.jsb.2010.03.007.

1201 82. Pettersen, E.F., Goddard, T.D., Huang, C.C., Couch, G.S., Greenblatt, D.M., Meng, E.C.,
1202 and Ferrin, T.E. (2004). UCSF Chimera—A visualization system for exploratory research
1203 and analysis. J. Comput. Chem. *25*, 1605–1612. https://doi.org/10.1002/jcc.20084.

1204 83. Emsley, P., Lohkamp, B., Scott, W.G., and Cowtan, K. (2010). Features and development of
1205 Coot. Acta Crystallogr. D Biol. Crystallogr. *66*, 486–501.
1206 https://doi.org/10.1107/S0907444910007493.

1207 84. Goddard, T.D., Huang, C.C., Meng, E.C., Pettersen, E.F., Couch, G.S., Morris, J.H., and
1208 Ferrin, T.E. (2018). UCSF ChimeraX: Meeting modern challenges in visualization and
1209 analysis. Protein Sci. *27*, 14–25. https://doi.org/10.1002/pro.3235.

85. Croll, T.I. (2018). ISOLDE: a physically realistic environment for model building into low-resolution electron-density maps. Acta Crystallogr. Sect. Struct. Biol. *74*, 519–530. https://doi.org/10.1107/S2059798318002425.

86. Adams, P.D., Afonine, P.V., Bunkóczi, G., Chen, V.B., Davis, I.W., Echols, N., Headd, J.J., Hung, L.-W., Kapral, G.J., Grosse-Kunstleve, R.W., et al. (2010). PHENIX: a comprehensive Python-based system for macromolecular structure solution. Acta Crystallogr. D Biol. Crystallogr. *66*, 213–221. https://doi.org/10.1107/S0907444909052925.

87. Afonine, P.V., Poon, B.K., Read, R.J., Sobolev, O.V., Terwilliger, T.C., Urzhumtsev, A., and Adams, P.D. (2018). Real-space refinement in PHENIX for cryo-EM and crystallography. Acta Crystallogr. Sect. Struct. Biol. *74*, 531–544. https://doi.org/10.1107/S2059798318006551.

88. Yu, R.C., Jahn, R., and Brunger, A.T. (1999). NSF N-Terminal Domain Crystal Structure: Models of NSF Function. Mol. Cell *4*, 97–107. https://doi.org/10.1016/S1097-2765(00)80191-4.

89. Joosten, R.P., Long, F., Murshudov, G.N., and Perrakis, A. (2014). The PDB_REDO server for macromolecular structure model optimization. IUCrJ *1*, 213–220. https://doi.org/10.1107/S2052252514009324.

90. Hamelryck, T., and Manderick, B. (2003). PDB file parser and structure class implemented in Python. Bioinformatics *19*, 2308–2310. https://doi.org/10.1093/bioinformatics/btg299.

91. Cock, P.J.A., Antao, T., Chang, J.T., Chapman, B.A., Cox, C.J., Dalke, A., Friedberg, I., Hamelryck, T., Kauff, F., Wilczynski, B., et al. (2009). Biopython: freely available Python tools for computational molecular biology and bioinformatics. Bioinformatics *25*, 1422–1423. https://doi.org/10.1093/bioinformatics/btp163.

92. Pedregosa, F., Varoquaux, G., Gramfort, A., Michel, V., Thirion, B., Grisel, O., Blondel, M., Prettenhofer, P., Weiss, R., Dubourg, V., et al. (2011). Scikit-learn: Machine Learning in Python. J. Mach. Learn. Res. *12*, 2825–2830.

93. Gowers, R.J., Linke, M., Barnoud, J., Reddy, T.J.E., Melo, M.N., Seyler, S.L., DomaÅ„ski, J., Dotson, D.L., Buchoux, S., Kenney, I.M., et al. (2016). MDAnalysis: A Python Package for the Rapid Analysis of Molecular Dynamics Simulations. In Proceedings of the 15th Python in Science Conference, S. Benthall and S. Rostrup, eds., pp. 98–105. https://doi.org/10.25080/Majora-629e541a-00e.

94. Jumper, J., Evans, R., Pritzel, A., Green, T., Figurnov, M., Ronneberger, O., Tunyasuvunakool, K., Bates, R., Žídek, A., Potapenko, A., et al. (2021). Highly accurate protein structure prediction with AlphaFold. Nature *596*, 583–589. https://doi.org/10.1038/s41586-021-03819-2.

95. Davis, I.W., Leaver-Fay, A., Chen, V.B., Block, J.N., Kapral, G.J., Wang, X., Murray, L.W., Arendall, W.B., Snoeyink, J., Richardson, J.S., et al. (2007). MolProbity: all-atom contacts

and structure validation for proteins and nucleic acids. Nucleic Acids Res. *35*, W375–W383. https://doi.org/10.1093/nar/gkm216.

96. Liebschner, D., Afonine, P.V., Baker, M.L., Bunkóczi, G., Chen, V.B., Croll, T.I., Hintze, B., Hung, L.-W., Jain, S., McCoy, A.J., et al. (2019). Macromolecular structure determination using X-rays, neutrons and electrons: recent developments in Phenix. Acta Crystallogr. Sect. Struct. Biol. *75*, 861–877. https://doi.org/10.1107/S2059798319011471.

97. Greaves, J., Gorleku, O.A., Salaun, C., and Chamberlain, L.H. (2010). Palmitoylation of the SNAP25 Protein Family. J. Biol. Chem. *285*, 24629–24638. https://doi.org/10.1074/jbc.M110.119289.

Acknowledgments

We thank Richard Held, Jeremy Leitz, Rama Ranganathan, Subu Subramanian, Benjamin White, Susan Wu, and Minglei Zhao for stimulating discussions; E. Montabana and C. Zhang for assistance with the electron microscopy data collection at the Stanford University cEMc; and Paul D. Adams, Pavel Afonine, and Nigel Moriarty for assistance with PHENIX refinement. Funding was provided by the US National Institutes of Health (NIH; RO1MH63105 to A.T.B.) and the Helen Hay Whitney Foundation/HHMI (to K.I.W.). Molecular graphics and analyses performed with *UCSF ChimeraX*, developed by the Resource for Biocomputing, Visualization, and Informatics at the University of California, San Francisco, with support from National Institutes of Health R01-GM129325 and the Office of Cyber Infrastructure and Computational Biology, National Institute of Allergy and Infectious Diseases. This article is subject to HHMI's Open Access to Publications policy. HHMI laboratory heads have previously granted a non-exclusive CC BY 4.0 license to the public and a sublicensable license to HHMI in their research articles. Pursuant to those licenses, the author-accepted manuscript of this article can be made freely available under a CC BY 4.0 license immediately upon publication.

Author contributions

K.I.W. and A.T.B. developed the research plan and experimental strategy. K.Q. and J.D. performed the cellular imaging experiments in PC12 cells and analyzed the data. Y.A.K. and A.B. performed the cellular imaging experiments in yeast and analyzed the data. K.I.W., Y.A.K. S.C., L.E., and R.P. purified all proteins. K.I.W., S.C., and Y.A.K. performed the disassembly experiments. K.I.W. performed the cryo-EM experiments and analyzed the data. K.I.W. and A.T.B. wrote the manuscript with input from the other authors.

Competing Interest Statement

All authors declare no competing interests.

Figures

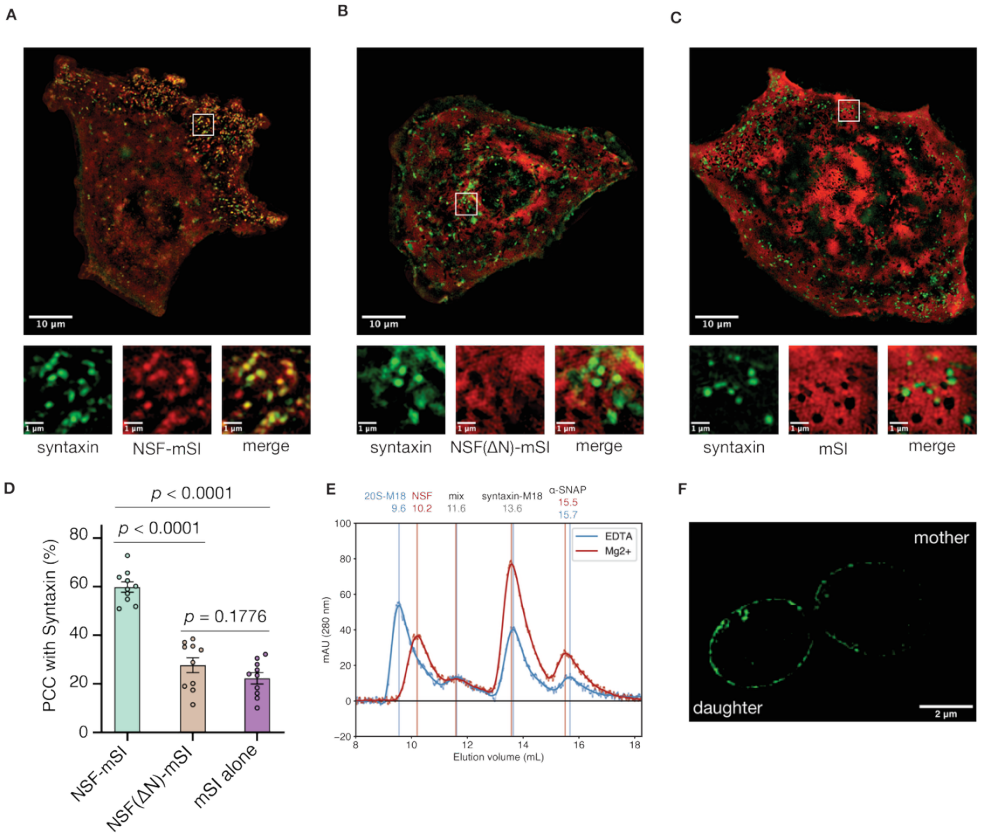

Figure 1 | NSF colocalizes to syntaxin nanodomains in an N-domain dependent manner and disassembles syntaxin oligomers

A. Colocalization between syntaxin-GFP nanodomains and NSF-mScarlet-I. NSF often forms clusters overlapping with syntaxin (PCC = 60% ± 2%, mean ± SEM).

B. Colocalization between syntaxin-GFP nanodomains and NSF(ΔN)-mScarlet-I; disruption of colocalization is evident (PCC = 28% ± 3%, mean ± SEM).

C. Colocalization between syntaxin-GFP and mScarlet-I alone. No interaction is apparent (PCC = 22% ± 2%, mean ± SEM).

1291 **D.** Comparison of NSF-mScarlet-I, NSF(ΔN)-mScarlet-I, and mScarlet-I clustering with
1292 syntaxin-GFP nanodomains (M ± SEM, n = 10 images). Statistical significance was established
1293 by two-tailed Student's t-tests. Colocalization between NSF-mScarlet-I and syntaxin-GFP is
1294 significantly different than between NSF(ΔN)-mScarlet-I and syntaxin-GFP ($p = 8.9002\times10^{-8}$) or
1295 between mScarlet-I and syntaxin-GFP ($p = 5.2106\times10^{-10}$). Colocalization between NSF(ΔN)-
1296 mScarlet-I and syntaxin-GFP and colocalization between mScarlet-I and syntaxin-GFP were not
1297 significantly different ($p = 0.1776$).

1298 **E.** To demonstrate disassembly tetrameric syntaxin-1a SNARE complexes by NSF and α-SNAP,
1299 and to show the insufficiency of Munc18 alone in disassembly, sx20S was prepared from
1300 purified components, split into two pools, resuspended in with a ~20-fold excess of Munc18.
1301 Following addition of EDTA or Mg^{2+}, pools were subjected to size-exclusion chromatography
1302 (SEC). Raw and filtered SEC profiles of the non-hydrolyzing (EDTA, blue) and hydrolyzing
1303 (Mg^{2+}, red) chromatograms at 290 nm are shown. The first peak corresponds to a complex of
1304 sx20S-Munc18 under non-hydrolyzing conditions (9.6 mL), or free NSF (10.2 mL) under
1305 hydrolyzing conditions. The second peak is consistent with an intermediate species of all
1306 proteins (11.6 mL). The third peak corresponds to a complex of syntaxin—Munc18 (13.6 mL),
1307 enriched twofold as assessed by integrated area under the curve (IAUC) under hydrolyzing
1308 conditions (12.8–14.8 mL; EDTA, 537.5 mAU^2; Mg^{2+}, 1058.5 mAU^2). The fourth peak is
1309 dominated by free α-SNAP, enriched twofold under hydrolyzing conditions (14.8–16.8 mL;
1310 EDTA, 224.4 mAU^2; Mg^{2+}, 442.7 mAU^2).

1311 **F.** Sso1p forms dense clusters in the *S. cerevisiae* plasma membrane during cell division as
1312 assessed by SIM. Sso1p clusters were enriched in the budding daughter cell (left); discrete
1313 clusters typically approached sizes near the Nyquist limit of 160 nm (n = 46 cell images).

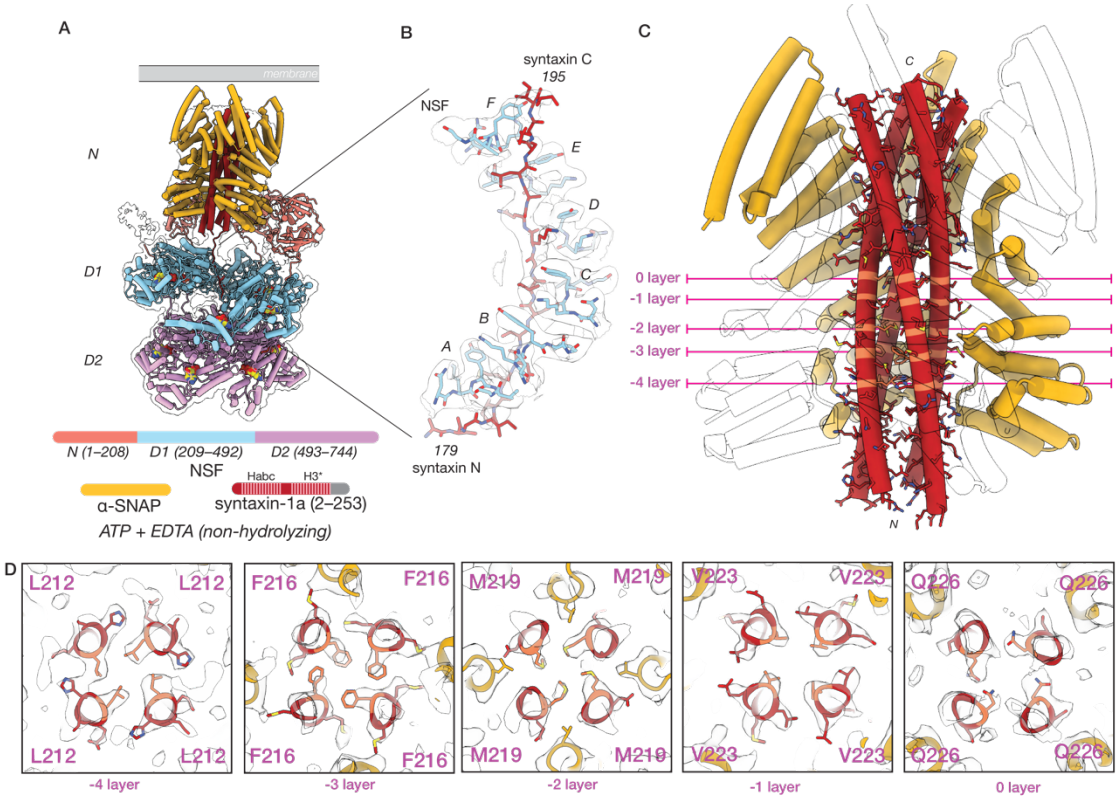

Figure 2 | NSF and α-SNAP engage a tetrameric SNARE complex composed of four syntaxin H3 domains

A. The structures of the sx20S (class #1, 3.75 Å) and the α-SNAP—syntaxin tetramer subcomplex (class #2, 4.07 Å). Hexameric NSF engages the α-SNAP—syntaxin tetramer subcomplex via its N-domains (salmon), several of which engage four α-SNAP molecules (gold) surrounding the soluble, tetrameric syntaxin H3 complex (dark red) within the catalytic D1 ring of NSF (light blue). The D2 ring of NSF (purple) does not engage the SNARE substrate. A hypothetical membrane is illustrated in grey. In the protein domain legend, ordered syntaxin domains are lightly shaded and those visible in the reconstruction of the SNARE complex are denoted with an asterisk; the syntaxin Habc domains were not observed.

1326 **B.** NSF (light blue) engages one of the four syntaxin molecules (dark red) in the tetramer via a
1327 series of pore loop interactions (protomers A–F, indicated); a tyrosine side chain (Y294) on each
1328 of the six protomers intercalates in between every other side chain of a portion of syntaxin N-
1329 terminal to its H3 domain. The corresponding sharpened map is contoured at 4 σ.

1330 **C.** The α-SNAP—syntaxin tetramer subcomplex model, with two of the four α-SNAP models
1331 hidden for clarity. The syntaxin H3 SNARE complex forms a twisted, parallel α-helical bundle
1332 with a series of key SNARE complex layers preserved.

1333 **D.** Slices through the α-SNAP—syntaxin tetramer subcomplex model and sharpened map at the -
1334 4–0 layers, with key residues lightened for emphasis. Each layer is characterized by nearly planar
1335 interactions between four identical side chains within the helical bundle. The primary
1336 interactions between α-SNAP and the syntaxin H3 complex are observed near the -2 and -3
1337 layers, where several functionally essential α-SNAP side chains (L197, Y200) are positioned by
1338 a loop that buries them within the groove of the bundle. No symmetry was imposed during

reconstruction.

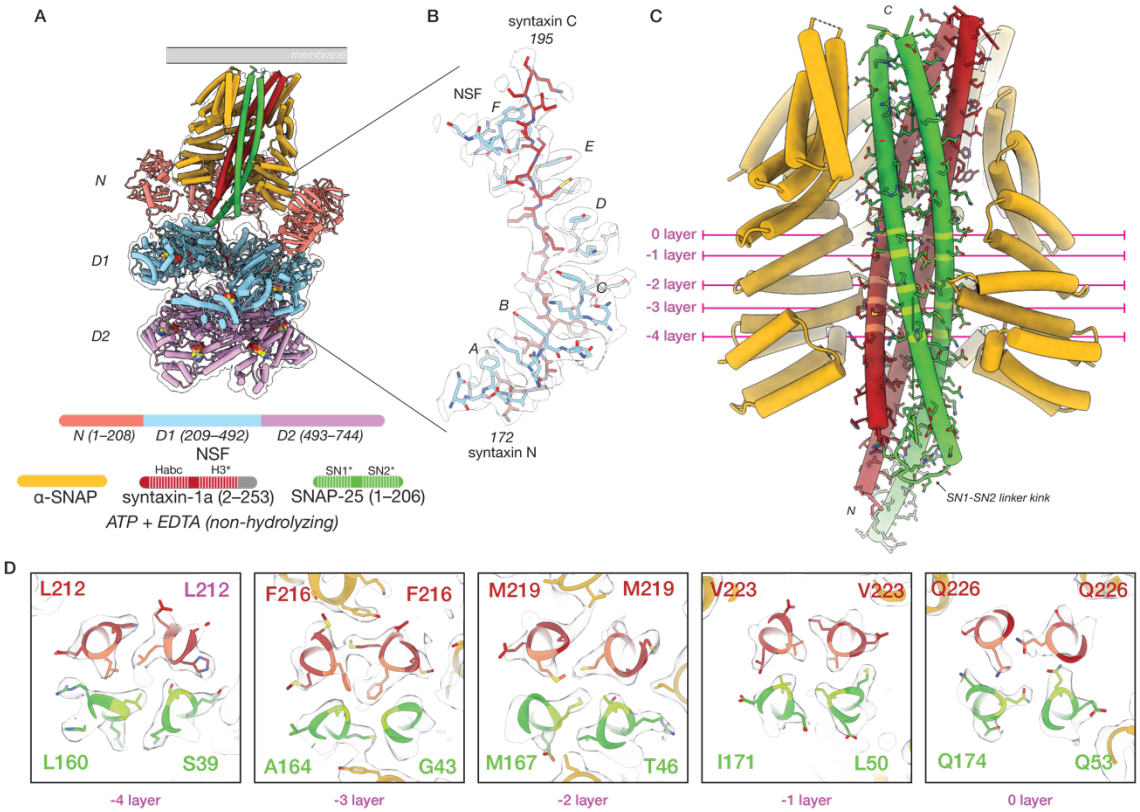

Figure 3 | NSF and α-SNAP engage a 2:1 binary SNARE complex of syntaxin H3 and SNAP-25 SN1 and SN2 SNARE domains under non-hydrolyzing conditions

A. A representative 21bin20S model (class #5, 3.39 Å) and α-SNAP—2:1 binary SNARE subcomplex model (class #13, 3.74 Å). Hexameric NSF engages the α-SNAP—2:1 binary SNARE subcomplex via multiple N-domains (salmon), which engage three α-SNAP molecules (gold) surrounding the 2:1 binary SNARE complex composed of two syntaxin H3 domains (dark red) and the SN1 and SN2 SNARE domains of a single SNAP-25 molecule (green). A linker N-terminal to one of the syntaxin H3 domains is found within the catalytic D1 ring of NSF (light blue). The D2 ring of NSF (purple) does not engage substrate. A hypothetical membrane is illustrated in grey. In the protein domain legend, ordered syntaxin and SNAP-25 domains are

1351 shaded and those visible in the reconstruction of the SNARE complex are denoted with an
1352 asterisk; syntaxin Habc domains were not observed.

1353 **B.** NSF (light blue) engages one of the two syntaxin molecules in the 2:1 binary SNARE
1354 complex (dark red) via pore loop interactions involving Y294 (protomers A–F, indicated). A
1355 sharpened map is shown, contoured at 5 σ. Of the eight 21bin20S classes with the 2:1 binary
1356 SNARE complex from the dataset collected under non-hydrolyzing conditions, six engage
1357 syntaxin and two engage SNAP-25 within the pore of the D1 ring.

1358 **C.** The α-SNAP—2:1 binary SNARE subcomplex model. Three α-SNAP molecules bind the 2:1
1359 binary SNARE complex; a flexible linker between SNAP-25 SN1 and SN2 blocks access by a
1360 fourth. The 2:1 binary SNARE complex forms a twisted, parallel α-helical bundle with a series
1361 of characteristic SNARE complex layers preserved. This configuration also places the N-
1362 terminal portion of the linker, bearing cysteines often palmitoylated *in vivo*, near the
1363 membrane[97].

1364 **D.** Layer slices through the α-SNAP—2:1 binary SNARE subcomplex model and sharpened
1365 map. Each layer is characterized by nearly planar interactions between four side chains within
1366 the helical bundle. The primary interactions between α-SNAP and the syntaxin H3 complex are
1367 found near the -2 and -3 layers, where several functionally essential[61] α-SNAP side chains (L197,
1368 Y200) are positioned by a loop that buries them within the bundle groove.

1369

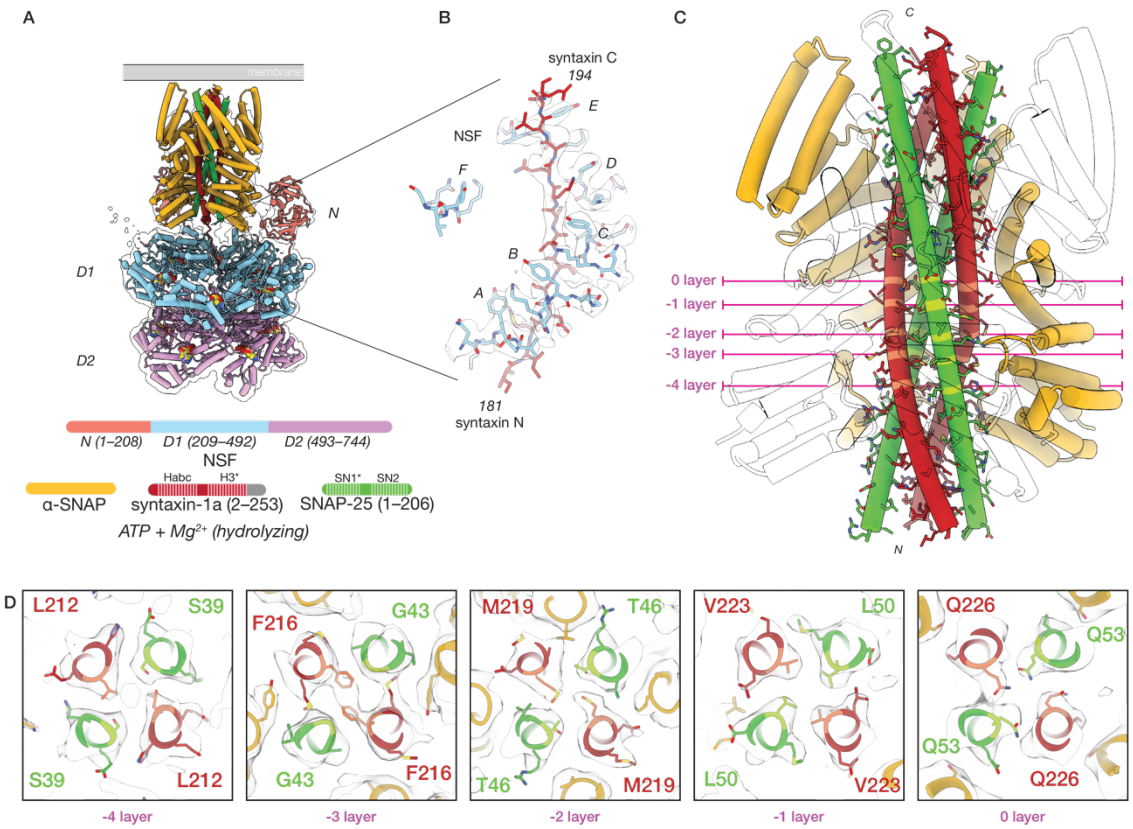

Figure 4 | NSF and α-SNAP engage a 2:2 binary SNARE complex of syntaxin H3 and SNAP-25 SN1 SNARE domains under hydrolyzing conditions

A. A representative 22bin20S model (class #19, 3.56 Å) and α-SNAP—2:2 binary SNARE subcomplex model (class #23, 4.14 Å). Hexameric NSF engages the α-SNAP—2:2 binary SNARE subcomplex via N-domains (salmon), which engage three α-SNAP molecules (gold) surrounding the soluble, 2:2 binary SNARE complex composed of two syntaxin H3 domains (dark red) and two SNAP-25 SN1 domains contributed by two separate full-length SNAP-25 molecules (green). A portion of a linker N-terminal to one syntaxin H3 domain is observed within the catalytic D1 ring of NSF (light blue). The D2 ring of NSF (purple) shows no substrate density. A hypothetical membrane is illustrated in grey. In the protein domain legend, ordered syntaxin and SNAP-25 domains are lightly shaded and those visible in the reconstruction of the

1382 SNARE complex are denoted with an asterisk; syntaxin Habc domains and SNAP-25 SN2
1383 domains were not observed.

1384 **B.** NSF (light blue) engages one of the two syntaxin molecules (dark red) in the 2:2 binary
1385 SNARE complex via pore loop interactions involving Y294 (protomers A–F, indicated). A
1386 sharpened map is shown, contoured at 6 σ. Of the five 22bin20S classes with the 2:2 binary
1387 SNARE complex, all are found with syntaxin in the D1 pore, while two are observed with the N-
1388 terminus of the SNAP-25 SN1 domain in the pore.

1389 **C.** The α-SNAP—2:2 binary SNARE subcomplex model. Four α-SNAP molecules bind the 2:2
1390 binary SNARE complex, with two SNAP-25 SN1 SNARE domains and two syntaxin H3
1391 domains. This configuration locates two independent N-terminal portions of the SNAP-25 linker
1392 bearing cysteine sidechains often palmitoylated *in vivo* near the membrane[97].

1393 **D.** Slices through the α-SNAP—syntaxin tetramer subcomplex at the -4–0 layers. Each layer is
1394 characterized by nearly planar interactions between four side chains within the helical bundle.
1395 The primary interactions between α-SNAP and the syntaxin H3 complex are found near the -2
1396 and -3 layers, where several functionally essential[61] hydrophobic α-SNAP side chains, L197 and
1397 Y200, are buried within the bundle groove. Symmetry was not enforced during local
1398 reconstruction. Note that the near-twofold symmetry of the bundle leaves some sidechain
1399 densities poorly defined.

1400

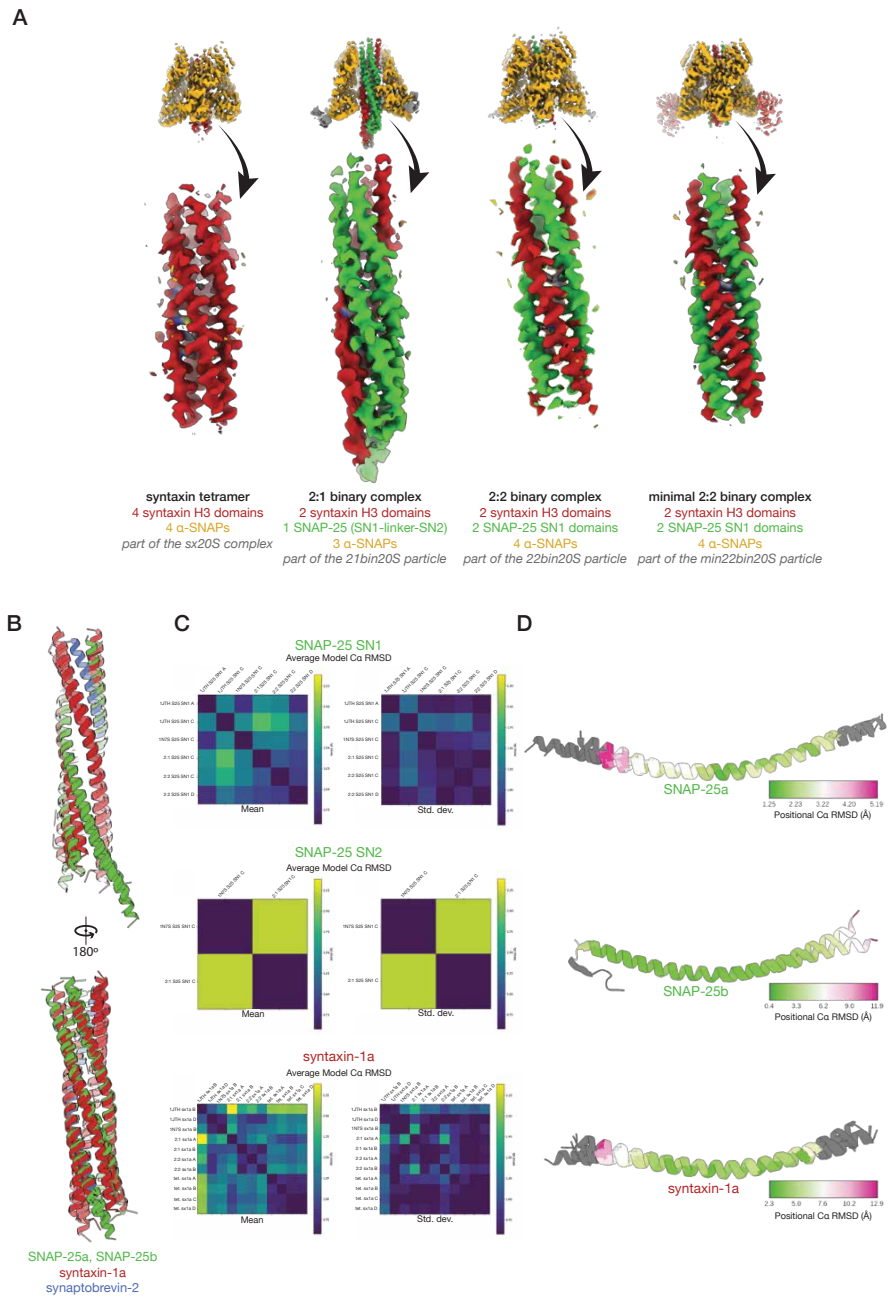

1401

1402 **Figure 5 | Reconstruction and comparison of SNARE complexes and sub-complexes**

1403 **A.** Signal subtraction and local refinement in *CryoSPARC*[80] produced reconstructions of four

1404 different α-SNAP—SNARE subcomplexes. In each case, the density of the SNARE proteins in

1405 the core of the subcomplex was sufficiently well-defined to assign the SNARE domain identity,
1406 directionality, and register.

1407 **B.** Crystal structures of the neuronal ternary SNARE complex (PDB ID 1N7S[54]) and the 2:2
1408 syntaxin—SNAP-25 complex (PDB ID 1JTH[34]) were superimposed using UCSF ChimeraX[84]
1409 with cryo-EM structures from this work of the tetrameric syntaxin H3 sub-complex, the 2:1
1410 syntaxin—SNAP-25 sub-complex, and the 2:2 syntaxin—SNAP-25 sub-complex within the
1411 bin20S complex. These structures show similar quaternary structure, maintaining the same
1412 register and similar twist in the central SNARE layers. The SNARE complexes and sub-
1413 complexes within their respective 20S complexes are somewhat untwisted at the N- and C-
1414 terminal ends relative to the crystal structures of the SNARE complexes alone, likely due to a
1415 combination of the absence of crystal packing as well as interactions with α-SNAPs and NSF.

1416 **C.** Quantitative comparison of individual SNARE domain ternary structure. Each pixel in a pair
1417 of matrices represents the mean Cα RMSD (Å, left) and corresponding standard deviation (right)
1418 between two instances of a given SNARE domain in two different structures. Only Cα atoms
1419 shared by all structures were considered. The same color scale is preserved across all
1420 comparisons. The mean Cα RMSD generally varies between 1–2 Å depending on the specific
1421 pair.

1422 **D.** Individual Cα RMSDs mapped to their corresponding SNARE domain structures, aligned.
1423 Core regions of the complexes are structurally similar, but unwinding near the SNARE domain
1424 termini leads to larger deviations, particularly near the N-termini where NSF engages one of the
1425 N-terminal segments leading into a SNARE domain (SNAP-25 or syntaxin).

1426

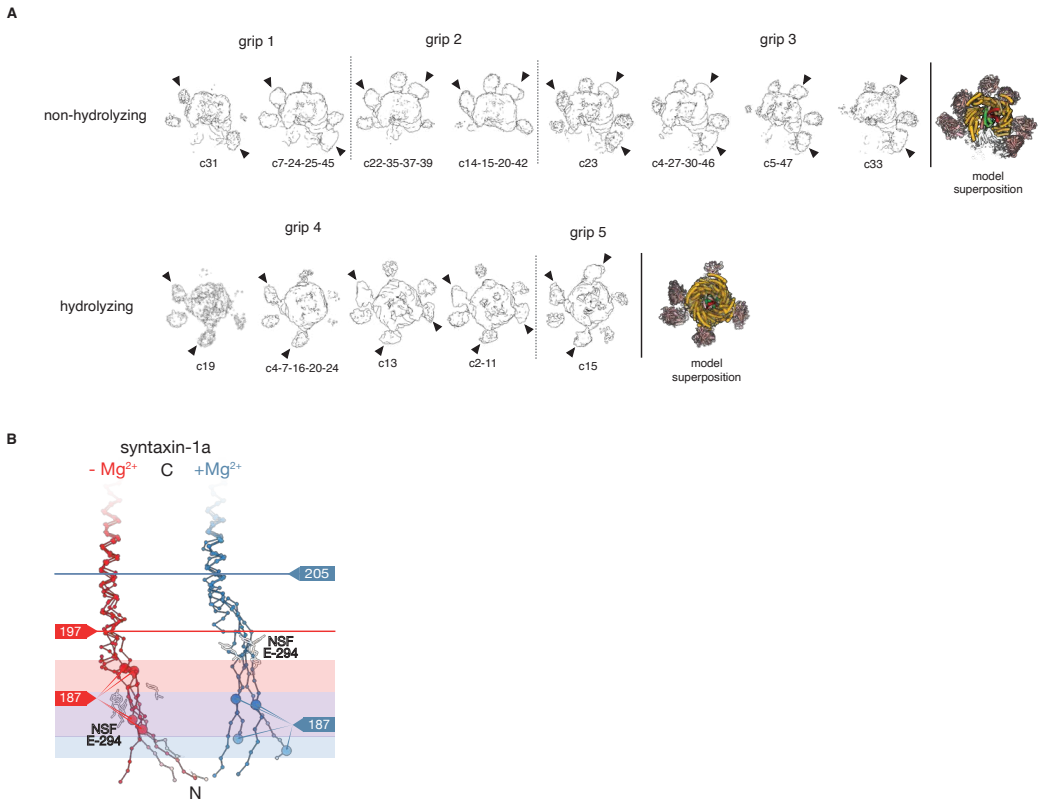

Figure 6 | Multimodal engagement of SNARE substrate by NSF

A. The α-SNAP—SNARE subcomplex is engaged by the NSF N domains. The orientation of the subcomplex relative to the NSF D1 ring split, the tilt of the subcomplex relative to the D1 ring, and the specific NSF N-domains engaged to the subcomplex are major determinants of particle class identity in different datasets. Three distinctive "grips" are observed in the case of the classes with the 2:1 syntaxin—SNAP-25 complex identified under non-hydrolyzing conditions (top), and two are observed in the case of the classes with the 2:2 syntaxin—SNAP-25 SNARE complex identified under hydrolyzing conditions (bottom). Pairs of N-domains typically bind a given α-SNAP near its C-terminus; arrows indicate the most well-ordered N-domains as assessed by the presence of two-lobed density. The two cases are not directly comparable, as the 2:1 syntaxin—SNAP-25 sub-complex is bound by three α-SNAP molecules, while the 2:2

1439 syntaxin—SNAP-25 sub-complex is bound by four α-SNAP molecules. This difference is likely
1440 due to the flexible linker that runs along the 2:1 syntaxin—SNAP-25 sub-complex surface
1441 between the SNAP-25 SN1 and SN2 SNARE domains. **B.** The SNARE N-termini are engaged
1442 by the NSF D1 pore. Variable syntaxin engagement by NSF between non-hydrolyzing and
1443 hydrolyzing classes is observed. Alignment of structures with ordered syntaxin substrates in the
1444 pore of the D1 ring under non-hydrolyzing (red) and hydrolyzing (blue) conditions reveals
1445 disruption of the syntaxin H3 domain up to around residues 197 and 205, respectively.

1446

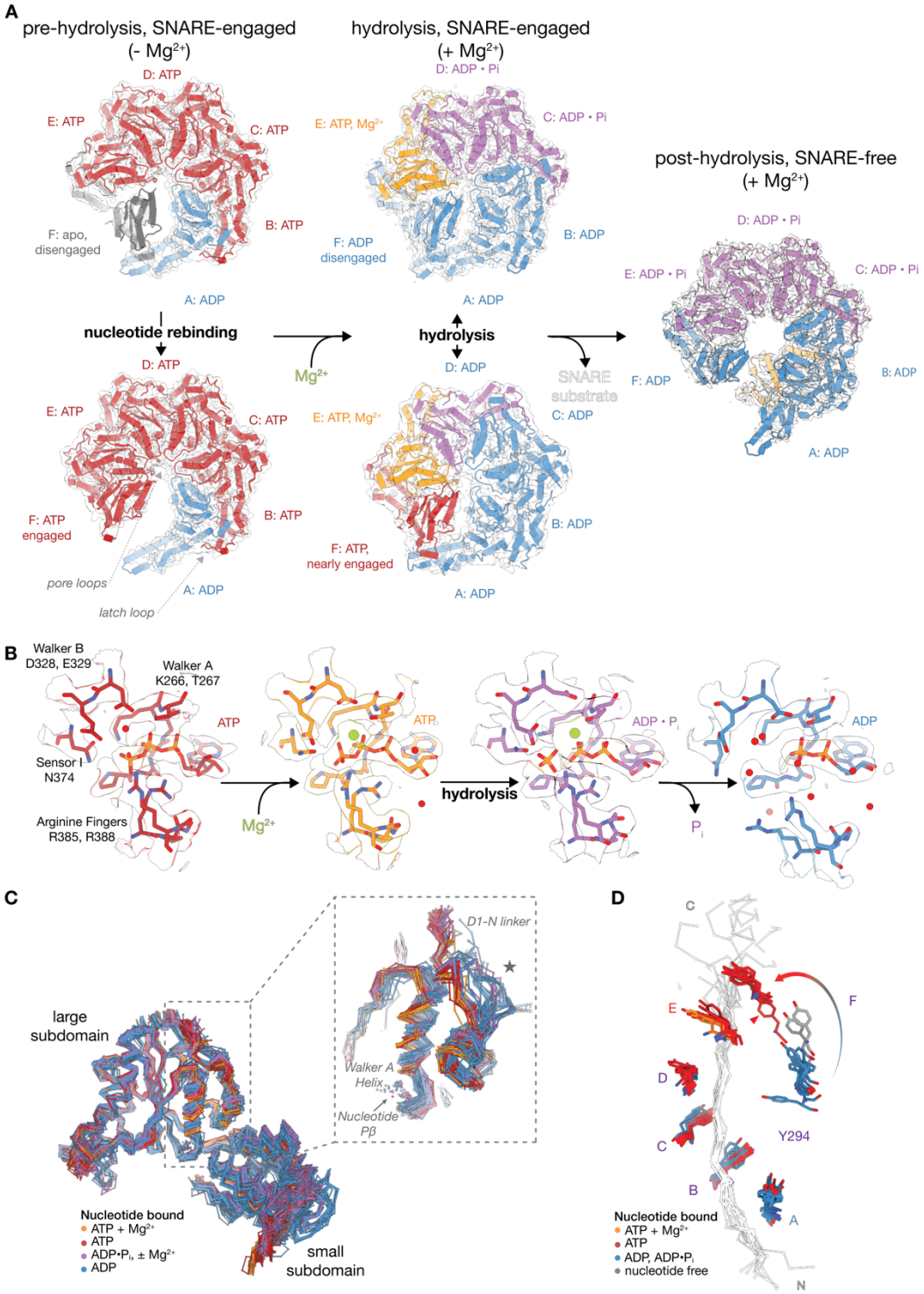

Figure 7 | Comparison of NSF structures under non-hydrolyzing and hydrolyzing conditions reveals the interplay between sequential AAA+ hydrolysis and substrate rebinding

1451 **A.** Key conformational states of the NSF D1 ATPase ring. Two states dominate in the absence of
1452 Mg^{2+} (left); the top class (#4) has SNARE substrate disengaged, nucleotide-free protomer F,
1453 while the bottom class (#3) has SNARE substrate-engaged, ATP-bound F. With the addition of
1454 Mg^{2+} (middle), E is Mg^{2+}-bound. Protomers D, C, and occasionally B retain P_i and Mg^{2+}.
1455 Protomers A are ADP-bound. The top subclass (#18) has substrate-disengaged, ADP-bound F.
1456 The bottom subclass (#17) has nearly substrate-engaged, ATP-bound F. Substrate-free, post-
1457 hydrolysis classes, e.g., #24 (right) show an ATP-free D1 ring. Spire, SNARE substrates, and the
1458 D2 ring are mostly hidden here.

1459 **B.** Details of hydrolysis. The P-loop binds nucleotide. Arginine fingers R385 and R388 from the
1460 down-ring protomer coordinate nucleotide phosphates. Without Mg^{2+}, a water molecule sits
1461 between the ɣ-phosphate and Walker B residue side chains of D328 and E329. Sensor 1 residue
1462 N374 is oriented towards the ɣ-phosphate of ATP. Under hydrolyzing conditions, Mg^{2+} is
1463 coordinated by the β- and ɣ-phosphate moieties of ATP and the side chain of Walker A motif
1464 T267. Following hydrolysis, ADP, P_i, and Mg^{2+} remain; Walker B E329 and Sensor 1 N374 side
1465 chains coordinate the P_i as it disassociates. P_i release down-ring leads to arginine finger
1466 disassociation, disrupting the interprotomer interface. Models are derived from D1 protomers #4-
1467 E, #16-E, #16-D, and #16-B.

1468 **C.** Alignment of 130 D1 protomer large subdomains from 23 models derived from all datasets.
1469 Only Cα and Pβ atoms are shown. The inset shows a key region of the protein that shows
1470 coupled changes in the N-D1 linker and the Walker A helix. The latch loop contributed by the up-
1471 ring protomer is also coupled to the conformational state of this region.

1472 **D.** Alignment of tyrosine residues in the pore of the D1 ring of substrate-bound models reveals
1473 protomer F as the site of nucleotide exchange and substrate re-engagement. ADP-bound F is
1474 disengaged from the substrate (blue). The release of ADP (nucleotide-free, grey) and ATP-
1475 binding (red) accompany substrate (re)engagement. The lowest tyrosine corresponding to an
1476 ATP-bound F shown (red triangle) is from the model shown in **A** (middle column, bottom).

1477

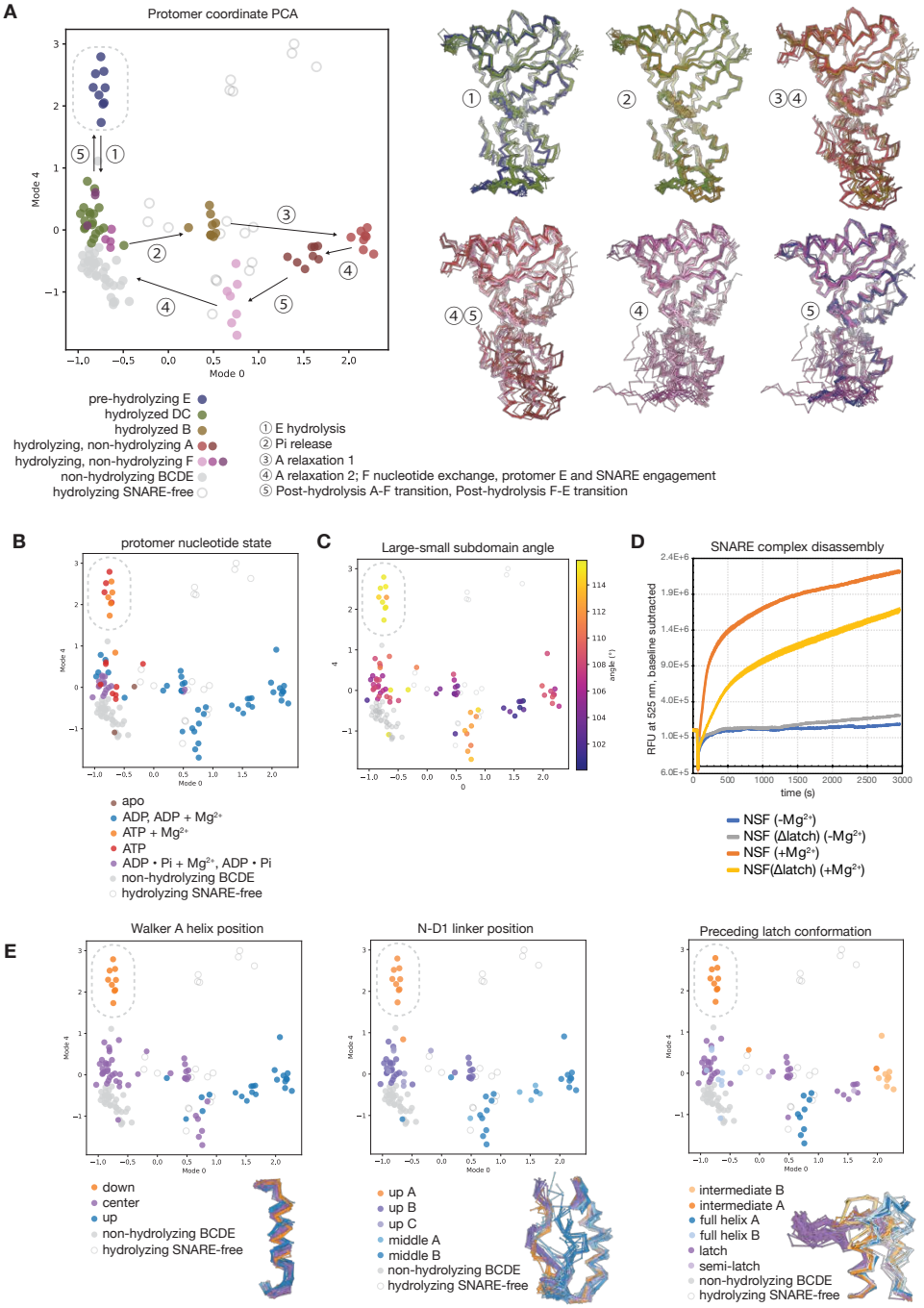

Figure 8 | Principal component analysis of NSF D1 protomer coordinates reveals quantitative mechanistic details of sequential hydrolysis

A. 132 D1 domain models were aligned by large subdomain, subjected to Cα coordinate PCA, and clustered with HDBSCAN in 11-dimensional space (left). Protomers cluster into discrete

1483 groups based on conformation, visible upon projection into a plane defined by the first and fifth
1484 modes. A proposed hydrolysis cycle is indicated. Superimposed models corresponding to these
1485 transitions are shown (right). The cluster corresponding to pre-hydrolysis protomers E is circled.

1486 **B.** Protomer nucleotide state, mapped to the 2D PCA coordinate from **A**. The ATP + Mg^{2+} state is
1487 unique to protomers E (circled).

1488 **C.** The angle (º) between helices α_3 and α_8 (a proxy for the relative angle between the D1 large
1489 and small subdomains). Protomers E have the largest angle (circled).

1490 **D.** A mutant form of NSF, NSF(Δlatch), in which part of the latch loop (residues 460–466) was
1491 replaced with a short glycine-serine linker (SGS), was assayed for its ability to disassemble the
1492 ternary SNARE complex composed of syntaxin, SNAP-25, and synaptobrevin[6]. Traces show the
1493 mean ± SEM of eight replicates for each form of NSF, with and without adding $MgCl_2$.
1494 Disassembly rates were calculated by linear regression to each trace in the linear region of the
1495 time course, from ~95–350 s. NSF(Δlatch) disassembled SNARE complex at 28 ± 1% the rate of
1496 wild type.

1497 **E.** Three conformational features distinguish the pre-hydrolysis protomer E cluster (circled).
1498 These features are in contact and structurally coupled. The position of nucleotide in the active
1499 site is modulated by the position of the Walker A helix (α_3), which occupies three discrete states;
1500 pre-hydrolysis protomers E occupy the "down" state (left). The position of the α_3 is allosterically
1501 modulated by at least two inputs. The N-D1 linker conformation (center) is connected to the state
1502 of N-domain binding to α-SNAP, and it interacts with the latch loop of the up-ring protomer
1503 upon rebinding. The latch loop of the up-ring protomer contacts this region in *trans* and is also

1504 structurally coupled (right). These two elements push against the C-terminal end of α_3 and

1505 ultimately modulate the position of the ATP γ-phosphate relative to key catalytic residues.

1506

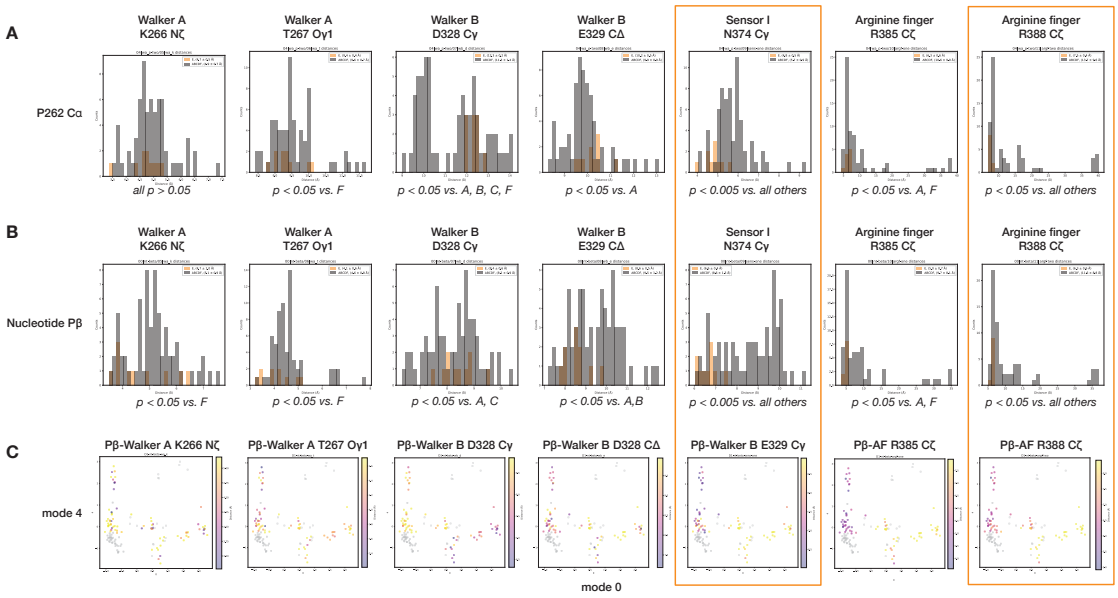

Figure 9 | The pre-hydrolysis state of protomers E has several unique active site features.

A. Distance distributions between the P262 Cα and a given active site residue. P262 Cα is a relatively invariant reference atom for measuring distances, as it is well-constrained by local geometry and the presence or absence of Pγ, Pi, or Mg^{2+} in the active site. Protomers E (orange bars) have a significantly closer Sensor I N374 distance to P262 (4.8 ± 0.5 Å vs. 5.7 ± 0.9 overall, $p < 0.005$ for all pairs) than any other protomer (black bars). The terminal carbon of the second arginine finger, R388 Cζ, was also significantly closer in protomers E than in any other protomer (7.5 ± 0.4 Å vs. 13.7 ± 9.6 Å, $p < 0.05$ for all pairs). While not a specific observation to protomer E, the P262 Cα-Walker B D328 Cγ distance distribution is bimodal, with ADP-bound protomers generally having a smaller distance between the two atoms. Welch's *t*-test, assuming unequal variances, was used to assess significance in all cases.

B. Distance distributions between the Pβ atom of either ATP or ADP of a given active site residue. Pβ was used as it is found in all nucleotide-bound protomers. The pattern of significant

differences between protomers E and protomers A–D and F described for P262 Cα is mostly repeated here, with the Sensor I N374 average distance to Pβ found to be highly significant (6.6 ± 0.4 Å vs. 8.6 ± 1.3, $p < 0.005$ for all pairs). As in **A**, the terminal carbon of the second arginine finger, R388 Cζ, was also significantly closer to Pβ in protomers E than in any other protomer (6.3 ± 0.6 Å vs. 11.6 ± 8.8, $p < 0.05$ for all pairs). Some differences are present in other cases. Aside from specific concerns related to protomers E, many of these distributions also show a bimodal pattern consistent with different nucleotide states. Welch's *t*-test, assuming unequal variances, was used to assess significance in all cases.

C. Distances from the histograms in **B** mapped to the coordinate determined by PCA.

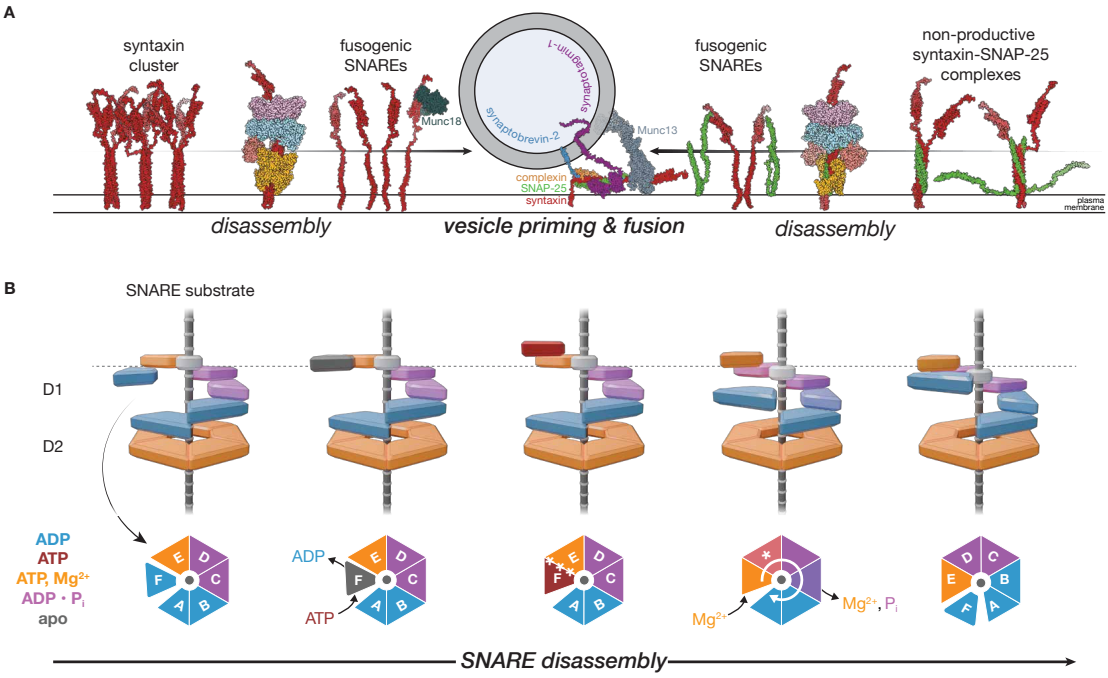

Figure 10 | An expanded model for NSF action across cellular and atomic scales

A. A model for disassembling non-fusogenic SNARE species by NSF and α-SNAP at the presynapse and progression to priming and fusion. Syntaxin nanodomains comprised at least in part of tetrameric syntaxin SNARE complexes serve as a reservoir for the liberation of individual, fusogenic syntaxin molecules by NSF upon disassembly. These syntaxin molecules may also enter non-productive binary complexes with SNAP-25, with 2:1 or 2:2 stoichiometry; such complexes would be disassembled by NSF to ensure *trans*-SNARE complex formation with synaptobrevin on incoming synaptic vesicles in concert with other factors, such as Munc18, Munc13, complexin, and synaptotagmin. Where possible, full-length structures (structures reported here and PDB IDs 1N7S, 4JEU, 5W5C) were supplemented with AlphaFold2[94] structures to provide additional context, and ISOLDE[85] was used with secondary structure restraints to reposition flexible regions.

1544 **B.** A sequential hydrolysis model for SNARE complex disassembly by NSF is inferred from
1545 comparing different classes from non-hydrolyzing and hydrolyzing conditions. Following
1546 hydrolysis-independent substrate side loading, the D1 ring is found in a pre-hydrolysis state with
1547 ATP in protomer E of D1. Protomer F nucleotide exchange then enables ATP exchange and
1548 rebinding to both SNARE substrate and the formation of the interprotomer interface with
1549 protomer E, triggering ATP hydrolysis in protomer E and substrate translocation. This is
1550 accompanied by P_i and Mg^{2+} release from down-ring protomers; in many structures, the release
1551 occurs between protomers C and B. The cycle then begins anew. Blue corresponds to ADP-
1552 bound, red to ATP-bound, purple to ADP•P_i bound, and grey to nucleotide-free. See Movie S1 for
1553 an animated rendition.

1554 Statistics and reproducibility

1555 No statistical method was used to predetermine the sample size, but experiments described in
1556 this study were performed with at least three samples for each group in the experiments shown
1557 throughout.

1558 Reporting summary

1559 Further information on research design is available in the Nature Portfolio Reporting Summary
1560 linked to this article.

1561